SANDIA REPORT

SAND2009-6998
Unlimited Release
Printed October 2009

Thermal Microphotonic Focal Plane Array (TM-FPA)

Applied Photonic Microsystems, Org. 1727
Michael R. Watts, Anthony L. Lentine, Peter T. Rakich, Jeremy B. Wright, David W. Peters, William A. Zortman, and Frederick B. McCormick

MEMS Core Technologies, Org. 1749-1
Michael J. Shaw

Advanced MEMS, Org. 1749-2
Gregory N. Nielson

Prepared by
Sandia National Laboratories
P.O. Box 5800, Albuquerque, New Mexico 87185

Sandia is a multiprogram laboratory operated by Sandia Corporation,
a Lockheed Martin Company, for the United States Department of Energy's
National Nuclear Security Administration under Contract DE-AC04-94-AL85000.

Approved for public release; further dissemination unlimited.

Sandia National Laboratories

Issued by Sandia National Laboratories, operated for the United States Department of Energy by Sandia Corporation.

NOTICE: This report was prepared as an account of work sponsored by an agency of the United States Government. Neither the United States Government, nor any agency thereof, nor any of their employees, nor any of their contractors, subcontractors, or their employees, make any warranty, express or implied, or assume any legal liability or responsibility for the accuracy, completeness, or usefulness of any information, apparatus, product, or process disclosed, or represent that its use would not infringe privately owned rights. Reference herein to any specific commercial product, process, or service by trade name, trademark, manufacturer, or otherwise, does not necessarily constitute or imply its endorsement, recommendation, or favoring by the United States Government, any agency thereof, or any of their contractors or subcontractors. The views and opinions expressed herein do not necessarily state or reflect those of the United States Government, any agency thereof, or any of their contractors.

Printed in the United States of America. This report has been reproduced directly from the best available copy.

Available to DOE and DOE contractors from
U.S. Department of Energy
Office of Scientific and Technical Information
P.O. Box 62
Oak Ridge, TN 37831

Telephone:	(865) 576-8401
Facsimile:	(865) 576-5728
E-Mail:	reports@adonis.osti.gov
Online ordering:	http://www.osti.gov/bridge

Available to the public from
U.S. Department of Commerce
National Technical Information Service
5285 Port Royal Rd
Springfield, VA 22161

Telephone:	(800) 553-6847
Facsimile:	(703) 605-6900
E-Mail:	orders@ntis.fedworld.gov
Online ordering:	http://www.ntis.gov/help/ordermethods.asp?loc=7-4-0#online

SAND2009-6998
Unlimited Release
Printed October 2009

Thermal Microphotonic Focal Plane Array (TM-FPA)

Abstract

The advent of high quality factor (Q) microphotonic-resonators has led to the demonstration of high-fidelity optical sensors of many physical phenomena (e.g. mechanical, chemical, and biological sensing) often with far better sensitivity than traditional techniques. Microphotonic-resonators also offer potential advantages as uncooled thermal detectors including significantly better noise performance, smaller pixel size, and faster response times than current thermal detectors. In particular, microphotonic thermal detectors do not suffer from Johnson noise in the sensor, offer far greater responsivity, and greater thermal isolation as they do not require metallic leads to the sensing element. Such advantages make the prospect of a microphotonic thermal imager highly attractive. Here, we introduce the microphotonic thermal detection technique, present the theoretical basis for the approach, discuss our progress on the development of this technology and consider future directions for thermal microphotonic imaging. Already we have demonstrated viability of device fabrication with the successful demonstration of a 20μm pixel, and a scalable readout technique. Further, to date, we have achieved internal noise performance ($\mathrm{NEP}_{Internal} < 1pW/\sqrt{Hz}$) in a 20$\mu$m pixel thereby exceeding the noise performance of the best microbolometers while simultaneously demonstrating a thermal time constant ($\tau = 2$ms) that is five times faster. In all, this results in an internal detectivity of $D^*_{internal} = 2 \times 10^9 \mathrm{cm} \cdot \sqrt{Hz}/\mathrm{W}$, while roughly a factor of four better than the best uncooled commercial microbolometers, future demonstrations should enable another order of magnitude in sensitivity. While much work remains to achieve the level of maturity required for a deployable technology, already, microphotonic thermal detection has demonstrated considerable potential.

Acknowledgement

The Sandia authors would like to thank Kevin Maschhoff, Steve Jost, and Andy Pomerene of BAE Systems for helpful comments related to thermal detector technology.

Contents

1 Microphotonic Thermal Detector Theory and Design **13**

Noise in Thermal Detection 14

Microphotonic Thermal Detection 14

Pixel Design 17

Silicon Nitride Detector Design 18

Microphotonic Thermal Imagers 21

Summary 23

2 Microphotonic Thermal Detector Fabrication **25**

Fabrication of a Silicon Detector 25

Fabrication of a Silicon Nitride Detector 27

Alternate Silicon Nitride Process 32

Summary 39

3 Experimental Results **41**

Measurement Apparatus and Methods 41

Internal Noise Performance 46

Summary 50

4 High resolution scalable readout technique for resonant optical sensors **53**

Introduction 53

Description of the Basic Technique 54

Extending the technique to multiple resonant detectors 56

Experimental Setup and Results. 58

Summary 60

References **60**

Appendix

A Method of Contacting a Microring-Resonator **63**

A.1 Background 63

A.2 Detailed Description of the Approach 64

List of Figures

1.1 (a) Diagram of a thermal microphotonic detector. The detector consists of a thermally isolated microphotonic resonator thermally coupled to an absorbing element and evanescently coupled to a bus waveguide. (b) In its simplest form, the readout consists of an interrogating laser sitting at the 3dB point of the resonance. Upon illumination, the temperature of the microresonator increases, shifting the resonant wavelength via the thermo-optic effect and a level change is sensed. 15

1.2 Comparison of detectivities of various high temperature infrared detectors. Note: present-day bolometer performance is almost two-orders of magnitude worse than could be achieved with an ideal thermal detector. 16

1.3 (a) Finite Element Model (FEM) of a silicon microring based thermal microphotonic detector. The supporting scaffold is constructed of silicon oxide. The outer diameter is $10\mu m$. The FEM thermal model demonstrates a thermal conductivity of $1.2x10^{-8}$ W/K. (b). Microring optical mode obtained by a Finite-difference cylindrical modesolver. The modesolver results indicate a silicon microresonator as small as R = 1.7μm can be utilized while maintaining a high-Q ($> 10^8$) optical mode. 18

1.4 (a) Finite Element Model (FEM) of a silicon-nitride microring based thermal microphotonic detector. The supporting and thermal insulating tethers are also constructed of silicon nitride and the entire structure is supported by an oxide post. The outer diameter is $20\mu m$. The FEM thermal model demonstrates a thermal conductivity of 1.2×10^{-7}W/K. (b). Microring optical mode obtained by a Finite-difference cylindrical modesolver. The modesolver results indicate a silicon-nitride microresonator as small as $R = 8\mu m$ can be utilized while maintaining a high-Q ($> 10^6$) optical mode. 19

1.5 Plot of optical constants for silicon nitride material used in the microring showing good extinction at wavelengths between 9 and 13 μm. The data in graph was measured by J. A. Woollam Co., Inc. with a IR-VASE® ellipsometer. 20

1.6 Absorption as modeled by 3D Rigorous Coupled Wave Analysis (RCWA) for a 200nm thick, 20μm diameter, silicon nitride disk suspended above a silicon substrate and normally incident radiation as a function of wavelength and separation from the silicon substrate. 21

1.7 Absorption as modeled by 3D Rigorous Coupled Wave Analysis (RCWA) for a 200nm thick, 20μm diameter, silicon nitride disk suspended above a tungsten coated substrate and normally incident radiation as a function of wavelength and separation from the substrate. 22

1.8 Concept for a thermal microphotonic focal plane array (TM-FPA). The TM-FPA approach depicted utilizes a WDM-based readout technique in order to interrogate columns of sensors. The resonances can be interrogated by simply stepping the laser to a 3dB point of the initial center wavelength of each column and reading out the amplitudes of transmission. 23

2.1 a) Idealized 3D model of Silicon on Insulator (SOI) microring design. b) fabricated microring. 25

2.2 Process steps required in fabricating a silicon microring TM-FPA. 26

2.3 a) SEM image of an oxidized silicon ring with silicon dioxide in place. b) SEM image of an oxidized silicon ring with silicon dioxide stripped away in HF, indicating the silicon tethers were completely oxidized. c) SEM image of a silicon ring created with the design shown in Table 1.1 with the silicon dioxide still in place. d) SEM images of the nanoscale tethers remaining after oxidation with the oxide stripped away in HF. . 27

2.4 a) 3D model of the silicon nitride microring design. b) Fabricated silicon nitride microring. 28

2.5 Array of uniform microrings demonstrating uniform undercut etch. 29

2.6 Process steps required in fabricating the silicon nitride microring TM-FPA sensor. Two dimensional (2D) renderings were generated with the Sandia 2D Process Visualizer, Version 2.35, generated from the photolithography mask design file drawn in AutoCAD^{TM}. 30

2.7 Interferometer reading of a nitride waveguide buckling over the open region of the evanescent coupler. 30

2.8 Measured resonance of a 20μm tethered silicon nitride microring resonator. 31

2.9 2D Process model representation of a cross section view of the new design using an alternate fabrication process flow. 32

2.10 Outline of process sequence to fabricate Gen2 TMFPA device. 33

2.11 Stress analysis of the oxide fin structure showing the buckling load versus fin thickness. 34

2.12 Block structures to preserve the waveguide during dicing. 35

2.13 Variation of trench depth using the same etch recipe. 35

2.14 Oxidation profiles for various oxidation times / thicknesses in silicon trenches. 36

2.15 Small voids appear in oxide fin structures after subjecting to HF chemistry. 36

2.16 Oxide fin fabrication strategies used to mitigate voides at the oxide to nitride interface and flare edge removal. 37

2.17 Incomplete release of suspended microring-resonator using the as-described alternate silicon nitride fabrication approach. 37

2.18 New design concepts to eliminate buckling in the tethers and etch release hole to insure complete release. 38

3.1 Apparatus used for test of thermal responsivity of microphotonic thermal sensor. Near IR Laser light (1550nm) is coupled into and collected from the microcavity within a vaccum chamber while a highly attenuated and modulated Mid IR (CO_2) laser signal diffusely illuminated the device through a transparent chamber window. When the microcavity resonance is properly excited by the 1550nm signal, the 1550nm signal is detected with an InGaAs PIN detector and analyzed with an oscilloscope and/or an RF spectrum analyzer. Calibration of the incident CO_2 laser signal is performed by introducing a calibrated (NIST traceable) pyroelectric detector in the CO_2 beam path. 42

3.2 (a) and (b) show the basic configuration by which $1550nm$ signals are coupled into and out of the chip using lensed fibers. The manner of flood illumination of the device is shown by the red colored areas. (c) Illustrates the manner in which the cavity resonance shifts when under illumination. The vertical dotted line shows the ideal manner of excitation of the microring for the purpose of detecting the this shift with optimal sensitivity. (d) Shows the resulting measured temporal modulation of the transmitted $1550nm$ signal (blue) which interacts with the ring along with the modulation of the CO_2 laser signal (seen in black). 43

3.3 Response of the pixel to a 30Hz square-wave modulated CO_2 laser signal incident on the pixel. An exponential fit to the time domain response indicates demonstrates an exponential time constant, τ = 2ms. This rapid response demonstrates applicability to a 240Hz frame-rate where the frame-rate is set to be approximately one over the rise time, i.e. $1/t_r$. 45

3.4 The frequency domain response of the pixel to a 100Hz square-wave modulation of the CO_2 laser indicating the external noise performance. the external noise performance is substantially limited by the poor IR absorption in the detector. 47

3.5 The frequency domain response of the pixel to a 100Hz square-wave modulation of the CO_2 laser. The internal noise performance of the detector demonstrates near phonon-noise limited performance. 49

3.6 Comparison of detectivities of various high temperature infrared detectors. The internal noise performance of the first microphotonic thermal detector exceeds the external noise performance of the best commercial bolometers. Considering the substantial advantage bolometers hold in development time / effort, this result is significant. 51

4.1 (a) Block diagram of the basic readout technique. (b) Spectrum of the modulated optical signal and the optical filter to select one sideband (c) Spectrum of a resonant sensor showing the shift from the applied stimulus relative to the reference position. The readout technique must measureΔ f. 54

4.2 Frequency response of many resonators in series. A wideband swept RF signal can be used to readout the positions of all the resonant nulls in one sweep. 56

4.3 Extension of the technique using WDM and parallelism to readout a large array of resonant sensors and the spectrum of the WDM/RF swept readout signal. 57

4.4 Block diagram of the experimental setup used to measure the repeatability of the frequency measurement capability 58

4.5 Traces from 64 sweep showing overlay on a wide-sweep (100 MHz) and a close up of a narrow sweep (100 kHz). Below the figures are shown the output data from the calculation showing a standard deviation of the measurement of only 11.7 kHz in the center frequency measurement. Number of averages = 1, Number of trials = 64 Threshold Mean = 37259.572 kHz, Std. Dev = 11.734 kHz, Max = 37284.250 kHz, Min = 37226.800 kHz 59

List of Tables

1.1 Material properties for the various materials detector materials where ρ, c_g, k, λ, and ν are the density, specific heat, thermal conductivity, elastic modulus, and Poisson's ratio, respectively 20

Chapter 1

Microphotonic Thermal Detector Theory and Design

Most focal plane array based optical imagers are formed from photon detectors where the incident radiation directly generates electron-hole pairs. Photon detectors achieve excellent noise performance when the photon energy is significantly greater than the thermal energy, $k_B T$. However, for wavelengths longer than a few micrometers, photon detectors must be cooled, often to cryogenic temperatures to minimize thermally induced transitions.

Alternatively, focal plane arrays can be formed from thermal detectors, where the incident radiation generates thermal energy inducing a temperature shift that is sensed through a change in some physical characteristic of the detector element, be it mechanical, electrical, optical or otherwise. While thermal noise is of course still problematic, fluctuations between states within a thermal detector do not typically degrade performance. The impact of thermal noise is therefore more controllable and room temperature operation of a thermal detector is possible, independent of photon energy. The development of microbolometer based focal plane arrays, which rely on the temperature coefficient of resistance to sense temperature excursions, have enabled high-resolution thermal images to be obtained at room temperature. This significant advance brought infrared and long-wave imaging to a wide-range of applications for which photon detectors do not exist or cryogenic cooling requirements limit their utility. Yet, despite over two-decades of development, the noise performance of microbolometers is insufficient for applications with long stand off distances. Moreover, microbolometer array sizes remain below one megapixel with pixels larger than 20μm significantly limiting both resolution and field of view. These limitations have opened the door for new classes of thermal imaging techniques.

One such technique is thermal microphotonic imaging [1]. Thermal microphotonic detection requires the combination of high-Q microphotonic resonators with extreme thermal isolation to ensure low-noise thermal detection. Further, an imager (i.e. focal plane array) will require yielding millions of microphotonic elements on a chip along with an equally scalable readout technique. In this Chapter, we review noise sources inherent to thermal detectors, present an approach for thermal microphotonic detection, and present one possible readout technique. Our goal is to inspire industry

researchers to consider thermal microphotonic imaging as an approach with potential to reach levels of performance previously attained only by cryogenically-cooled detectors.

Noise in Thermal Detection

Fundamentally, all thermal detectors are limited by thermal phonon fluctuations due to energy exchange with a thermal bath (e.g. the substrate) [2][1]. This energy exchange, described by Gibbs [3], is classical in origin (analogous to Brownian motion) and cannot be distinguished from absorbed radiation. The resultant noise equivalent power (NEP) of this background flux is given by $NEP_{phonon} = \sqrt{4k_B G T}$, where k_B is Boltzmann's constant, G is the thermal conductance to the substrate, and T is the temperature. Assuming room temperature operation, the only free parameter is the thermal conductance. For thermal conductances $G = 10^{-7}$W/K, 10^{-8}W/K and 10^{-9}W/K, the thermal phonon noise levels are $NEP_{phonon} = 7 \times 10^{-13}$W/$\sqrt{}$Hz, 2×10^{-13}W/$\sqrt{}$Hz, and 7×10^{-14}W/$\sqrt{}$Hz, respectively. The later NEP is in the vicinity of cryogenically cooled photon detectors.

In addition to the unavoidable thermal phonon fluctuations, bolometers suffer from Johnson noise, $1/f$ noise, and a small responsivity (i.e. $\frac{1}{R}\frac{dR}{dT} \sim 0.02/K$). Moreover, due to the opposing goals of achieving low thermal conductance and high electrical conductance, the best microbolometers achieve $G \sim 10^{-7}$W/K. The best microbolometer noise floors are NEP $> 10^{-12}$W/$\sqrt{}$Hz (often $\sim 10^{-11} W/\sqrt{Hz}$), close to an order of magnitude higher than their phonon noise floors, and almost two orders of magnitude higher than what might be possible in a more ideal thermal detector.

Microphotonic Thermal Detection

A thermal microphotonic detector consists of a bus waveguide, a thermally isolated microresonator, and an absorbing element in thermal contact with the microresonator (see Fig. 1.1a). The bus waveguide is critically coupled to the microphotonic resonator so as to ensure complete extinction on resonance. The absorber converts incident optical power to thermal power causing a rise in temperature in both the absorber and the resonator. For a given absorbed power level, P, the temperature rise is P/G, where G is the thermal conductance from the resonator to the substrate. This temperature rise shifts the resonance through the thermo-optic effect, as depicted in Fig. 1.1b. The shift can be detected by a laser line operating at one of the 3dB

[1]Secondarily, all detectors are limited by photon fluctuations from blackbody radiation in the background, but the noise level resulting from the photon fluctuations tends to be lower than the phonon fluctuations and is both wavelength and system dependent.

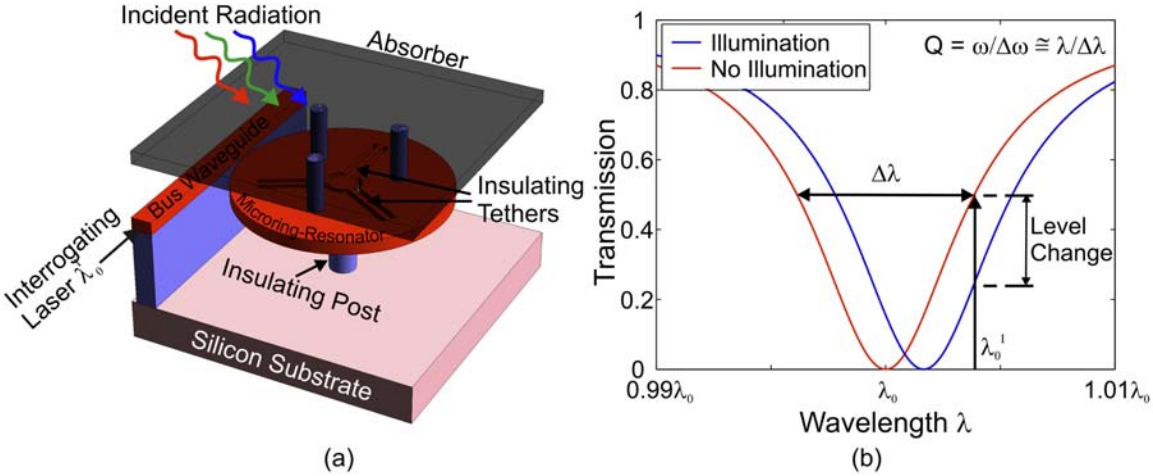

Figure 1.1. (a) Diagram of a thermal microphotonic detector. The detector consists of a thermally isolated microphotonic resonator thermally coupled to an absorbing element and evanescently coupled to a bus waveguide. (b) In its simplest form, the readout consists of an interrogating laser sitting at the 3dB point of the resonance. Upon illumination, the temperature of the microresonator increases, shifting the resonant wavelength via the thermo-optic effect and a level change is sensed.

points of the resonance. The fractional change$\Delta\ S$ in signal S for a given amount of absorbed power, (i.e. the responsivity) is given by

$$\frac{\Delta S}{S \cdot P} = -\frac{Q}{G}\frac{d\lambda_0}{\lambda_0 dT} \tag{1.1}$$

where λ_0 is the resonant wavelength and we have made the approximation $Q = \frac{\omega_0}{\Delta\omega} \approx \frac{\lambda_0}{\Delta\lambda}$. Assuming a Q of 10^6 and a thermal conductance of $G = 10^{-7}$W/K, cavities constructed of silicon nitride and silicon have responsivities that are ∼600 and ∼2,500 larger than microbolometers, respectively. By itself, this is significant, but the advantage is even more substantial when we consider the fact that no electrical contacts need to be made to the sensor. With only dielectric supports connecting the sensor to the substrate, thermal conductances of $G = 10^{-8}$W/K are certainly possible, and 10^{-9}W/K may be realizable, further enhancing the scale factor and reducing the thermal fluctuations. In addition to the significant advantages of scale factor and greater thermal isolation, microphotonic detectors do not suffer from Johnson noise in the sensing element, do not have significant $1/f$ noise components, and need not be perturbed by the interrogating signal. All of these traits point to the potential to measure thermal fluctuations two-orders of magnitude below present day microbolometer performance. In addition, by using high index contrast materials,

pixel sizes can be reduced to $\sim 5\mu$m, which not only enhances resolution but also improves the thermal response for high speed applications.

A chart of the performance of existing detector technologies is depicted in Fig. 1.2. In the visible and near-infrared region of the spectrum (0.4-to-2μm) detector performance is exceptional even without cooling. In the mid-infrared (3-to-5μm) region of the spectrum, the performance degrades, but with a moderate degree of cooling the performance of HgCdTe detectors is still quite good. In the long-wave (8-to-12μm), the performance of photon detectors is poor without cryogenic cooling ($T = 77$K). To realize uncooled detectors, a switch from photon detectors to thermal detectors must be employed. Yet, the performance is far away from the background limit even for the best uncooled thermal detectors, microbolometers. Of the electromagnetic spectra, it is clear that thermal detectors are most competitive in the long-wave regions of the spectra for which no high performance uncooled photon detectors exist.

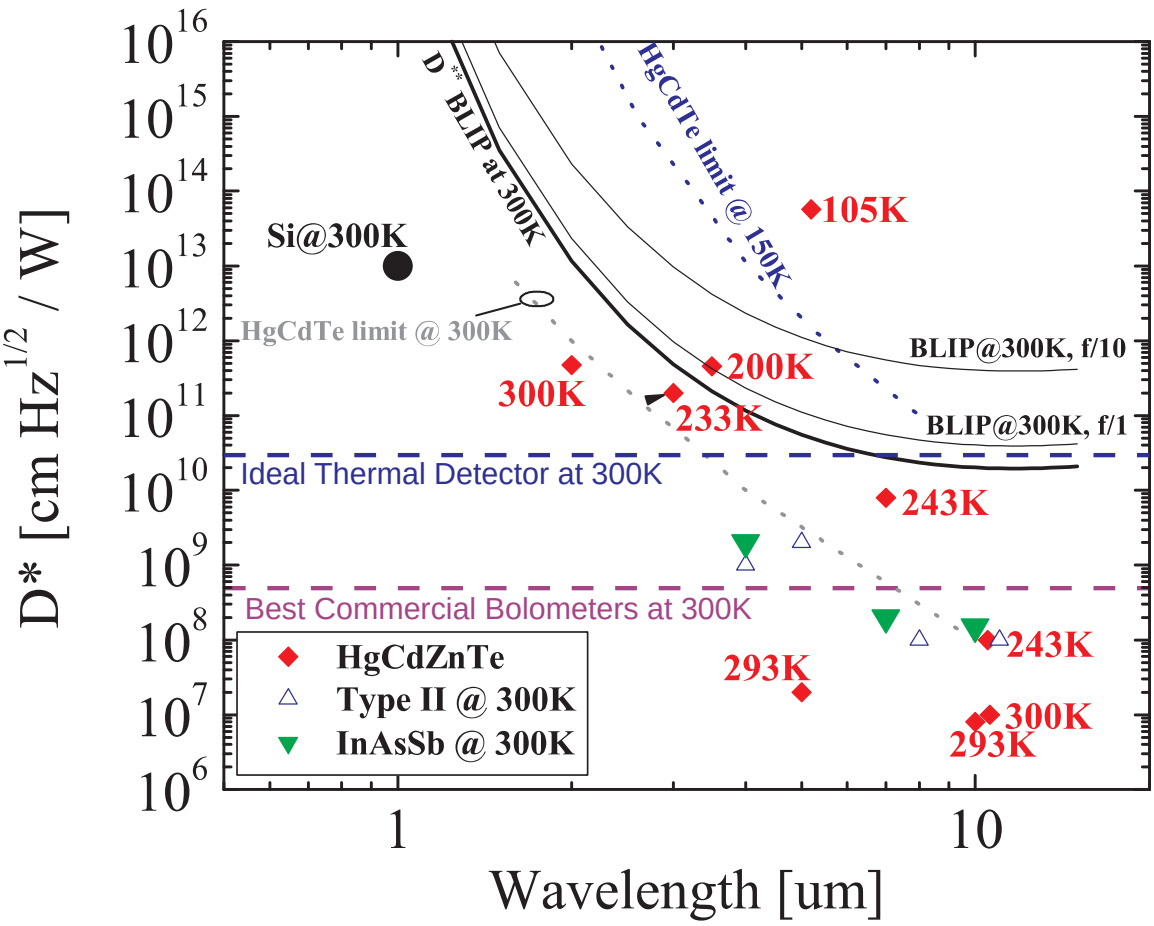

Figure 1.2. Comparison of detectivities of various high temperature infrared detectors. Note: present-day bolometer performance is almost two-orders of magnitude worse than could be achieved with an ideal thermal detector.

Pixel Design

When considering pixel design, there are four principal requirements that need to be met: (1) pixel pitch that is on the order of the wavelength of light to be detected, (2) high resonator quality factor, (3) a high degree of thermal isolation, and (4) strong absorption in the wavelength range of interest.

Since the long-wave infrared region of the spectrum is of primary interest, pixels sizes on the order of 10μm are required. This means that when designing a microphotonic thermal detector, very small resonant cavities must be employed. Of demonstrated resonant cavity geometries, the microring-resonator offers the best combination of high quality factor and small size. To achieve very small size, however, high index contrast materials must be employed. Of the high index contrast materials available in a CMOS fabrication facility, silicon and silicon nitride, are both prevalent, and have demonstrated low-loss propagation at telecom wavelengths ($\lambda \sim 1.5\mu$m).

Silicon offers the highest of index contrasts and therefore the smallest potential pixel sizes. It is therefore a highly interesting material to consider. However, silicon does have some drawbacks. One of the principal challenges with using silicon for a thermal detector material is its high thermal conductivity. To overcome this challenge, we have developed a pixel design that utilizes a silica scaffold to isolate the pixel from the substrate. This design is presented in Fig. 1.3a. The supporting scaffold in this case is composed of the in-plane concentric rings with supports connecting the rings, and the post that extends down to the substrate. The in-plane support structure provides 90-to-95% of the thermal resistance in the structure. Conduction through the silicon oxide scaffold to the substrate was determined by a finite element model (FEM). The ring has an outer radius of 5.0μm and an inner radius of 4.55μm. The finite element thermal model indicates that the thermal conductance is 1.2×10^{-8}W/K. Since mechanical vibration can induce resonant frequency changes through deformation of the structure and interaction with the bus waveguide, we used the mechanical model to determine the resonance of the structure. Fortunately, the lowest mechanical resonant frequency of this structure was found to be greater than 1 MHz. Because of this high resonant frequency, neither environmental acoustic vibrations nor thermally induced mechanical vibrations will likely disturb the sensing signal. The silicon / silicon-oxide structure demonstrates that very low thermal conductivities can be achieved with proper design. Moreover, it is likely that the thermal conductivity is in fact lower than we are reporting since finite-size effects have not yet been taken into account. In Fig. 1.3b, the optical mode of a highly confined silicon microring-resonator is presented. The mode was calculated using a finite-difference cylindrical modesolver and found to have a $Q > 10^8$ with a radius of only $1.7\mu m$ illustrating the very small pixel dimensions that are possible with thermal microphotonic detectors constructed of silicon microring-resonators. A pixel pitch as small as 5μm is certainly possible. While silicon microrings enable very small pixel sizes, silicon has some disadvantages: (1) it does not absorb strongly in the long-wave infrared, (2) it has a very high thermal conductivity, and (3) it suffers from

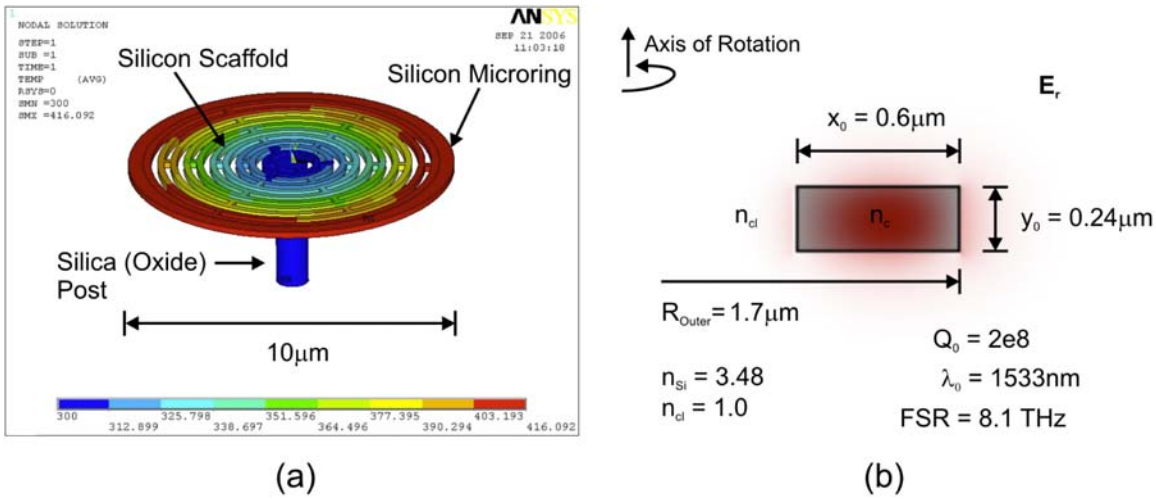

Figure 1.3. (a) Finite Element Model (FEM) of a silicon microring based thermal microphotonic detector. The supporting scaffold is constructed of silicon oxide. The outer diameter is $10\mu m$. The FEM thermal model demonstrates a thermal conductivity of $1.2x10^{-8}$ W/K. (b). Microring optical mode obtained by a Finite-difference cylindrical modesolver. The modesolver results indicate a silicon microresonator as small as R = 1.7μm can be utilized while maintaining a high-Q ($> 10^8$) optical mode.

large nonlinearities. The challenges can likely be overcome, but present roadblocks for early demonstrations. It is therefore worth considering alternatives. Of the high index materials within a CMOS fabrication facility, silicon nitride is among the most prevalent and well understood.

Silicon Nitride Detector Design

While silicon nitride is a lower index material than silicon and therefore does not enable pixel sizes that are quite as small, it has some inherent advantages: (1) it is transparent at 1.55μm, but absorbs strongly from 8-to-12μm, (2) it has a very low thermal conductivity in thin film form, (3) it can be deposited in low loss form, and (4) it possesses only very weak nonlinearities. For these reasons, silicon nitride is a natural material to consider. A baseline design for a silicon nitride detector microphotonic thermal detectors has been developed. The design includes a large region of silicon nitride to act as an infrared absorber. The design also incorporates a silicon nitride microring with silicon nitride tethers and a silicon dioxide insulating post for thermal isolation. A diagram and finite element thermal model of the microphotonic detector design is provided in Fig. 1.4a. Since silicon nitride has a lower index than silicon,

the optical ring resonator requires a larger diameter. A finite-difference cylindrical modesolver was used to determine the optical mode and an acceptable radius for maintaining the resonator quality factor. The modesolver results (Fig. 1.4b) indicate that a quality factor of $Q > 10^6$ is achievable with a device radius of only 6μm. To be conservative, we chose a diameter of 20μm for the thermal simulation in Fig 1.4a. The FEM determined thermal conductance is $1.2 \cdot 10^{-7}$ W/K. In addition, thin film values for the thermal conductivity of silicon nitride have been reported to be significantly lower (as low as 0.8W/(K·m)) than the bulk value (as low as 16W/(K·m)) used in this analysis and it is likely that these lower thermal conductivities are a result of finite-size effects. Therefore, these results are conservative. The lowest mechanical resonant frequency of this structure is 420 kHz, lower than that for the silicon detector, but still very high. Environmental and/or thermally induced mechanical vibrations should not be a significant factor in the performance of the structure.

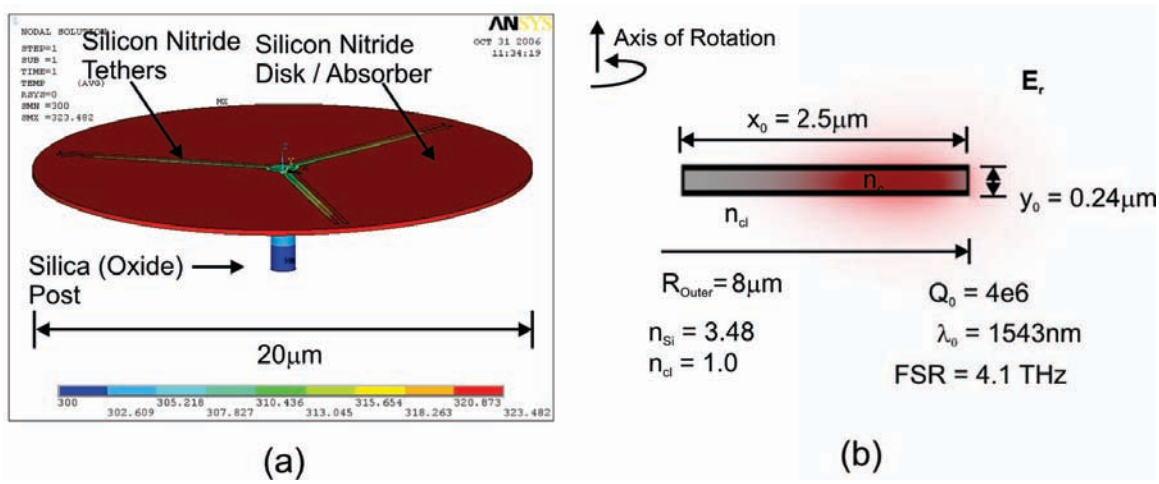

Figure 1.4. (a) Finite Element Model (FEM) of a silicon-nitride microring based thermal microphotonic detector. The supporting and thermal insulating tethers are also constructed of silicon nitride and the entire structure is supported by an oxide post. The outer diameter is $20\mu m$. The FEM thermal model demonstrates a thermal conductivity of 1.2×10^{-7}W/K. (b). Microring optical mode obtained by a Finite-difference cylindrical modesolver. The modesolver results indicate a silicon-nitride microresonator as small as $R = 8\mu m$ can be utilized while maintaining a high-Q ($> 10^6$) optical mode.

As mentioned previously, one of the primary benefits of using silicon nitride as a resonator material is that it turns out that while silicon nitride is transparent at $1.5\mu m$ where the resonance is being interrogated, it absorbs strongly from about 9-to-$13\mu m$ making it nearly ideal for long-wave infrared applications. The absorption for an as deposited stoichiometric silicon nitride film was measured by J. A. Woollam Co., Inc. using ellipsometry and the extracted real, n, and imaginary, k, indices of

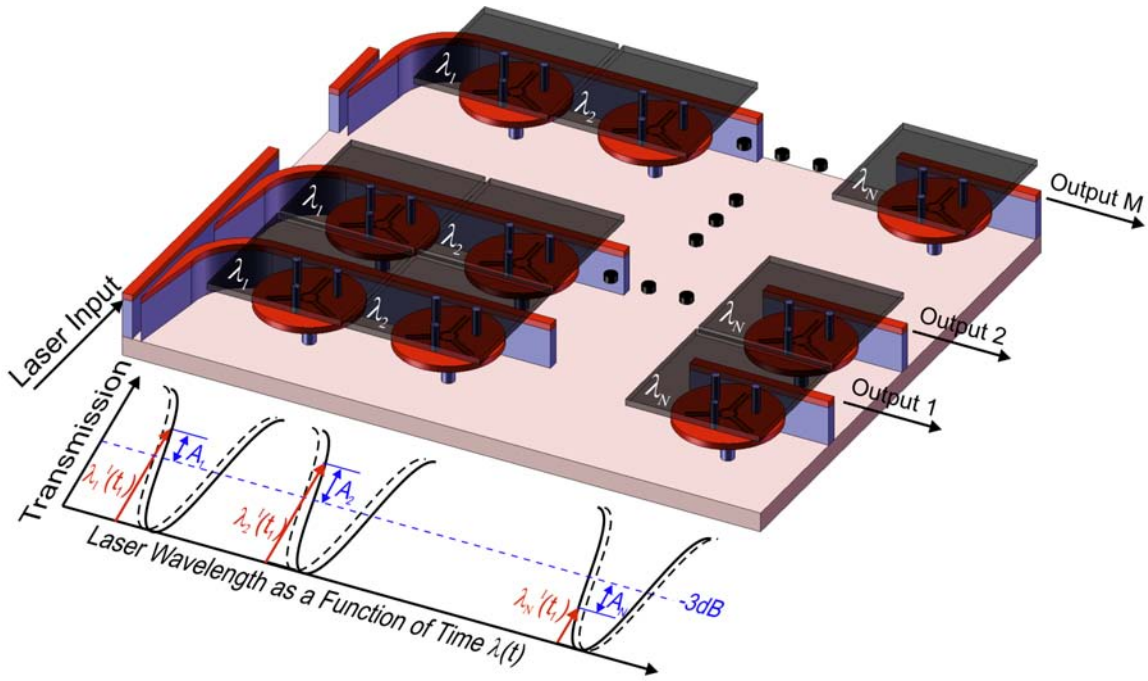

Figure 1.8. Concept for a thermal microphotonic focal plane array (TM-FPA). The TM-FPA approach depicted utilizes a WDM-based readout technique in order to interrogate columns of sensors. The resonances can be interrogated by simply stepping the laser to a 3dB point of the initial center wavelength of each column and reading out the amplitudes of transmission.

Summary

Challenging an established technology is inherently difficult. Unforeseen advances in microbolometer or alternate thermal imaging techniques could negate the current opportunity. Still, the seemingly clear inherent advantages of microphotonic thermal detection, in terms of scale factor, thermal noise levels, pixel size, and response time, make for a compelling case to develop single detector elements. Scaling to an array presents many additional challenges, but if addressed, significantly improved thermal imaging performance is likely to result. In the subsequent chapters, we describe our efforts to fabricate the detectors, measure their performance, and establish a high fidelity readout approach.

	ρ (kg/m^3)	c_g (J/kg·K)	k (W/m·K)	λ (GPa)	ν
Silicon	2330	712	148	160	0.2
Silicon Oxide	2220	745	1.38	69	0.17
Silicon Nitride	2400	691	16	270	0.27

Table 1.1. Material properties for the various materials detector materials where ρ, c_g, k, λ, and ν are the density, specific heat, thermal conductivity, elastic modulus, and Poisson's ratio, respectively

refraction are presented in Fig. 1.5. The fraction of incident light absorbed by the

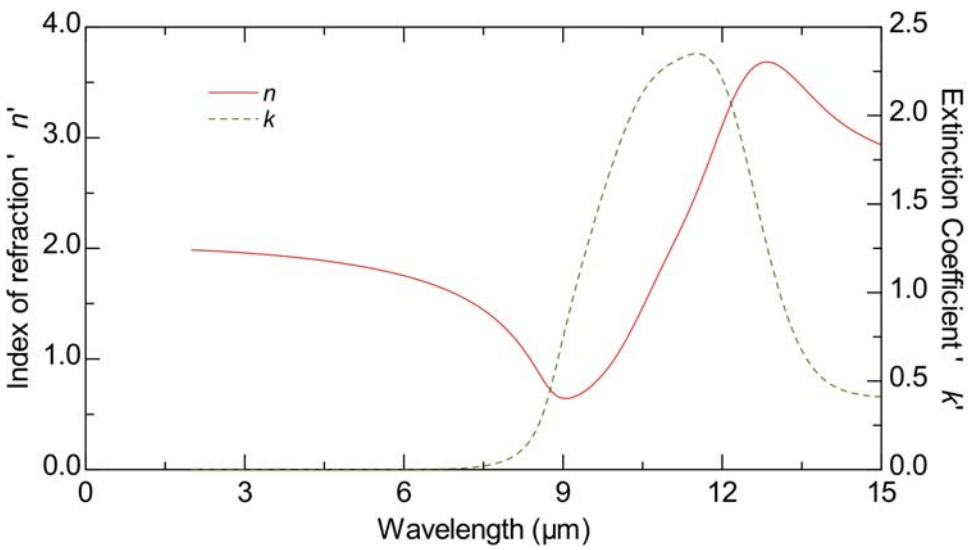

Figure 1.5. Plot of optical constants for silicon nitride material used in the microring showing good extinction at wavelengths between 9 and 13 μm. The data in graph was measured by J. A. Woollam Co., Inc. with a IR-VASE® ellipsometer.

silicon nitride detector was modeled using three-dimensional rigorous coupled wave analysis (RCWA). RCWA is an electromagnetic code that utilizes periodic boundary conditions. So, in the simulations, a periodicity must be assumed which is reasonable since most detectors will be utilized in arrayed imaging applications. For the case of a 20μm detector disk, we assumed a periodicity of 25μm to allow space for the interrogating bus waveguide. The absorption was then modeled as function of separation of the disk from a silicon substrate. The results of the RCWA simulations are presented in Fig. 1.6. The absorption increases substantially when the separation between the disk and the substrate is set to $\lambda/4$ and when a metallic coating is applied to the

substrate as demonstrated by coating the substrate with tungsten (Fig. 1.7).

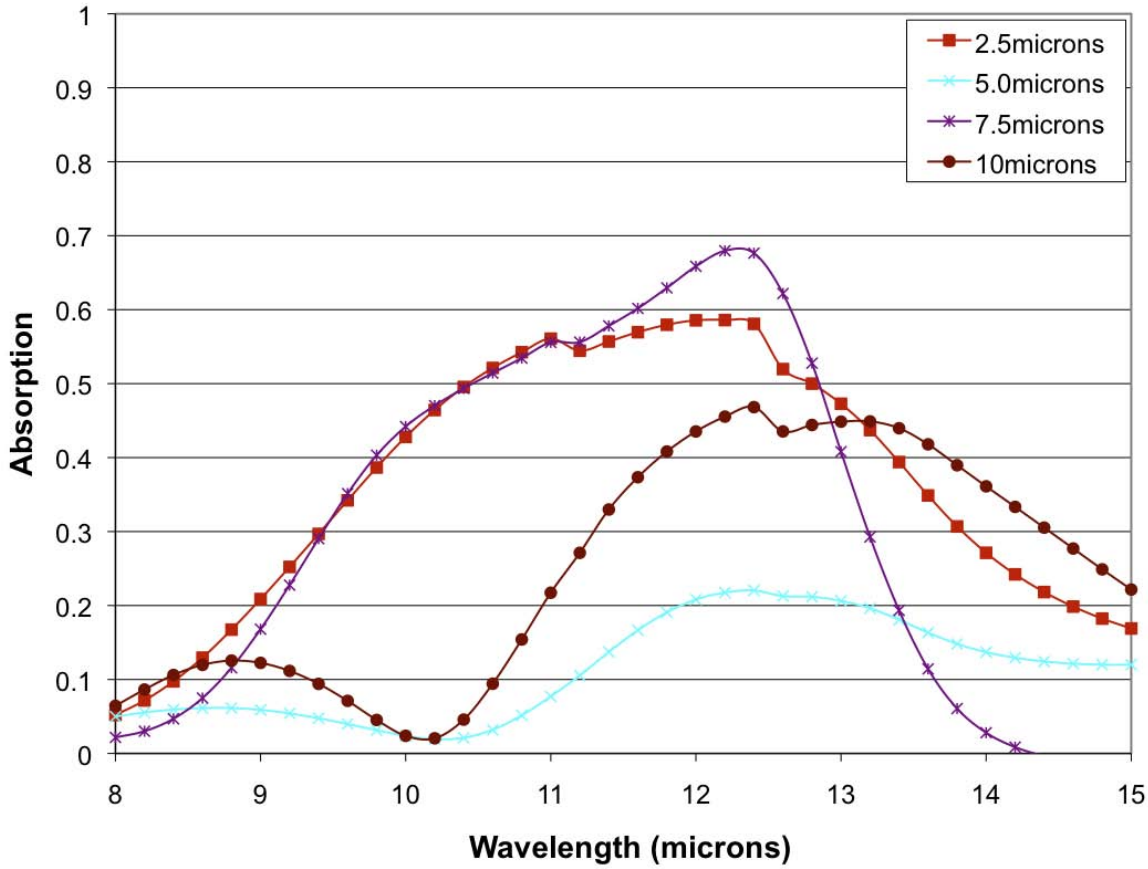

Figure 1.6. Absorption as modeled by 3D Rigorous Coupled Wave Analysis (RCWA) for a 200nm thick, 20μm diameter, silicon nitride disk suspended above a silicon substrate and normally incident radiation as a function of wavelength and separation from the silicon substrate.

Microphotonic Thermal Imagers

Scaling from a prototype sensor to a working thermal microphotonic focal plane array (TM-FPA) will certainly require significant effort. Principal among the challenges will be a scalable and reliable readout approach. At least a pair of readout techniques for interrogating microphotonic pixels can be envisioned. Pixels could be switched with MEMs-based switching techniques. Alternatively, a wavelength division multiplexed (WDM) approach could be employed. A WDM approach is attractive because it does not significantly burden the already complex fabrication process. A variety of WDM methods can be used to interrogate the microphotonic resonances, but to be consistent we consider the approach of measuring the amplitude of transmission

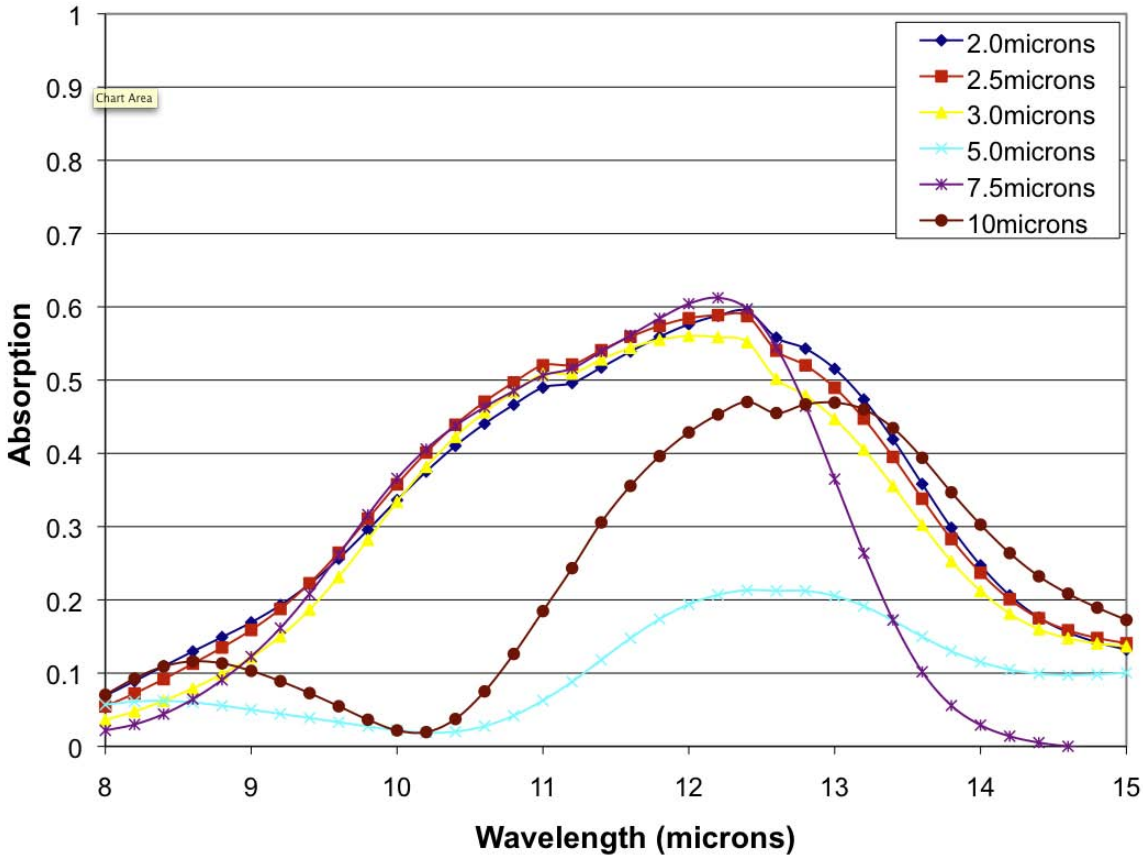

Figure 1.7. Absorption as modeled by 3D Rigorous Coupled Wave Analysis (RCWA) for a 200nm thick, 20μm diameter, silicon nitride disk suspended above a tungsten coated substrate and normally incident radiation as a function of wavelength and separation from the substrate.

depicted in Fig. 1.1. In this example, columns of pixels are fabricated to specific resonant wavelengths. A laser input is tapped to each row to enable simultaneous readout of a column of pixels. The laser wavelength is then scanned or stepped across all of the center wavelengths in the array. For this approach, the wavelength is stepped to a 3dB point of the initial center wavelength λ_i^I of a column. Since each pixel in the column will have a resonant wavelength that has been altered slightly by the absorbed radiation, the transmission of each will differ. The detected level for each pixel will then indicate the relative power absorbed. In this manner, each column is addressed and read out. Alternatively, as described in Chapter 4, the timing of the 3dB crossings can be used to establish the resonant frequencies of each of the pixels. This latter approach does not require an analog-to-digital converter, a considerable advantage compared to present day readout integrated circuits for microbolometers and HgCdTe detector arrays.

Chapter 2

Microphotonic Thermal Detector Fabrication

Implementing a large focal plane array will require yielding a million or more suspended microphotonic resonators with low-loss and precise frequency control. There is no doubt that doing so is likely to be a highly challenging undertaking. This Chapter details our efforts to fabricate high-quality microphotonic thermal detectors in a manner that ultimately enables scalability to large focal plane arrays.

Fabrication of a Silicon Detector

Our first microphotonic thermal detector design was the silicon detector, presented in Fig. 1.3 (also shown below in Fig. 2.1a). To review, the supporting scaffold in this structure is composed of the in-plane concentric rings with supports connecting to the rings, and the post that extends down to the substrate. As presented previously, the in-plane support structure provides 90-to-95% of the thermal resistance in the structure, enabling a predicted ultralow thermal conductance of 1.2×10^{-8}W/K.

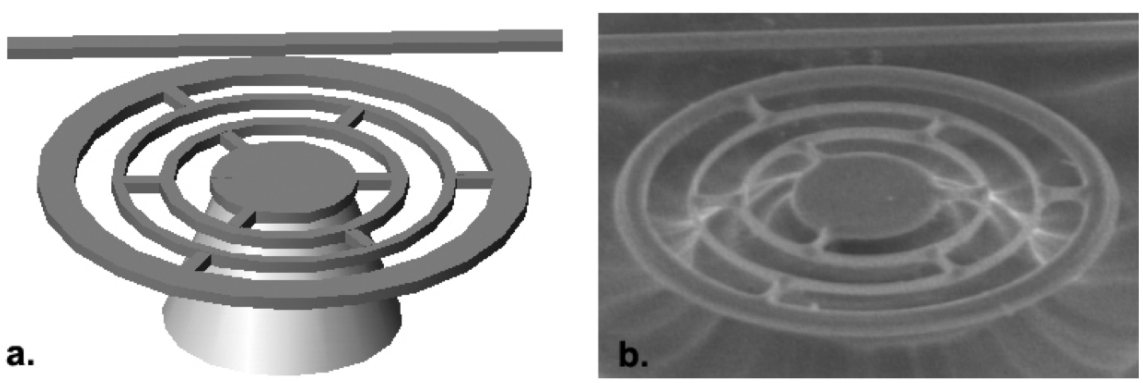

Figure 2.1. a) Idealized 3D model of Silicon on Insulator (SOI) microring design. b) fabricated microring.

To realize the silicon detector design, single crystal silicon microring waveguides were created from SOI wafers with a 0.5 μm device layer with a 3.0 μm buried oxide (BOX) layer that were purchased from Soitec Inc.. Details of the process flow are illustrated in Fig. 2.2. The two dimensional (2D) renderings were generated with the Sandia 2D Process Visualizer, Version 2.35, generated from the photolithography mask design file drawn in AutoCAD ™. The fabrication of the silicon rings was performed by etching the pattern in the SOI silicon layer, applying a silicon nitride hard mask to the patterned structures, and patterning the outer ring opening for the wet isotropic undercut etch. The silicon ring undercut was similar in uniformity as in the silicon nitride case and the final suspended structure was oxidized in steam to cause the tethers to become a thermally insulating lattice of high quality silicon dioxide as can be seen in Fig. 2.3a.

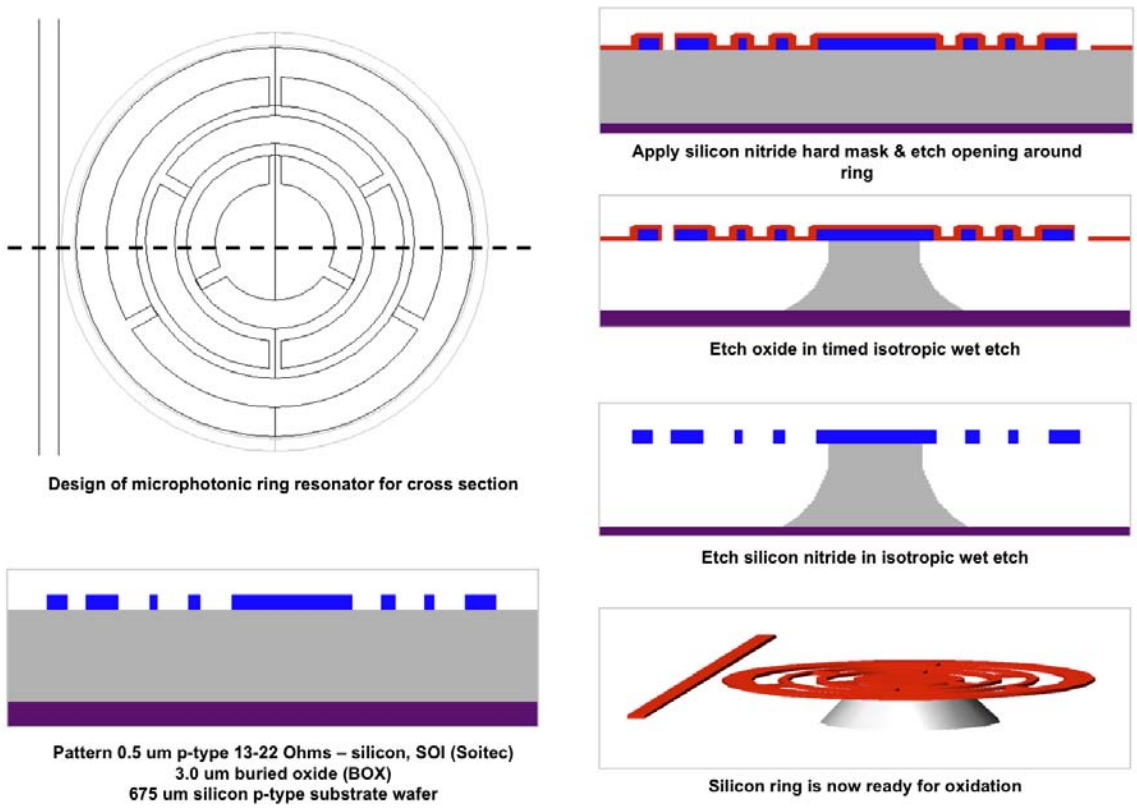

Figure 2.2. Process steps required in fabricating a silicon microring TM-FPA.

The silicon bus and microring waveguide were designed large enough to only partially oxidize and would remain encased in an oxide cladding. Images in Fig. 2.3c and 2.3d show the fine nano structures left behind in the tether regions of the silicon rings after oxidation and stripping of the oxide in Hydrofluoric acid (HF). No silicon ring devices fabricated according to the design shown in 2.3 survived the wet processing to remove the outer thermal oxide as indicated in Fig. 2.3b. This indicates that the

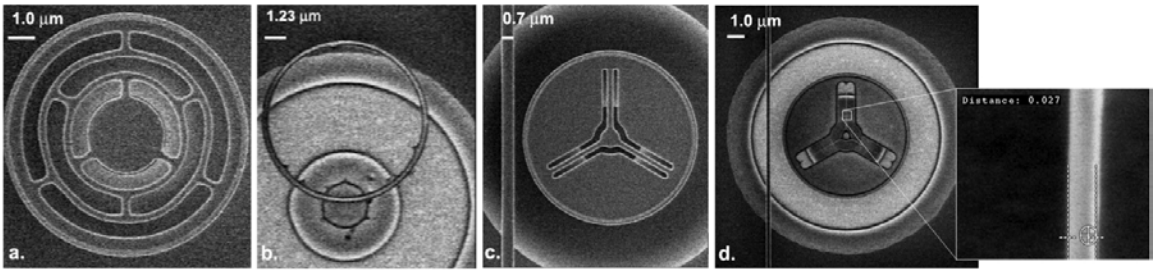

Figure 2.3. a) SEM image of an oxidized silicon ring with silicon dioxide in place. b) SEM image of an oxidized silicon ring with silicon dioxide stripped away in HF, indicating the silicon tethers were completely oxidized. c) SEM image of a silicon ring created with the design shown in Table 1.1 with the silicon dioxide still in place. d) SEM images of the nanoscale tethers remaining after oxidation with the oxide stripped away in HF.

silicon in the tethers was completely oxidized as intended or that whatever silicon remained was so small it was broken in the wet processing.

Thermally grown silicon oxide develops a significant compressive residual stress. If unconstrained, as in the case of the undercut tethers, a linear growth of about 22% is expected. The deflection in the tethers shown in Fig. 2.3a is a result of this expansion. The design of the tethers allowed for this deflection and it is clear that the structure behaved as intended and also supported the ring. Fig. 2.3c, the oxidized tethers also support the ring on the oxide post but some silicon remains un-oxidized. Fig. 2.3d shows the remaining nano tethers after the HF strip process where the un-oxidized silicon is only 27nm wide.

Despite some initial success in the fabrication of silicon microphotonic thermal detectors, the challenges in fabrication, coupled with the lack of an integrated infrared absorbing material and limited resources caused us to reconsider our initial detector material choice.

Fabrication of a Silicon Nitride Detector

As detailed in the previous chapter, on account of its transparency at the interrogation wavelength $\lambda = 1.5\mu$m, strong absorption in the long-wave infrared (LWIR), and low thermal conductance in thin film form, silicon nitride makes for a near ideal microphotonic thermal detector material. Further, Sandia has considerable experience in low loss silicon nitride waveguide technology having demonstrating microring resonators with Q's greater than 100,000 [8] a number of years ago. Moreover, the materials and processes required to create silicon nitride low loss wave-guides are

commonly found in standard integrated circuit fabrication facilities. To achieve the lowest loss, high temperature processes have proven most successful. Process strategies must accommodate these high temperatures before diffusion sensitive materials are introduced. While silicon nitride waveguide core material is typically clad with silicon dioxide, to create the microphotonic thermal detector depicted in Fig. 1.4 (and replicated below in Fig. 2.4a), a fully air-clad structure must be employed. A scanning electron microscope (SEM) image of a fabricated device is depicted in Fig. 2.4b. Both stoichiometric silicon nitride and low stress nitride (LSN), (i.e. silicon rich silicon nitride), waveguide materials were investigated in the initial fabrication attempts. The stoichiometric silicon nitride material proved to be a better choice than the LSN material due to limitations in the photo resist (PR) thickness, reactive ion etch (RIE) capability, and material losses. LSN was also shown in a previous study to have higher optical loss. The fine details required in the fabrication of these devices required the use of an ASML scanner stepper with a minimum resolution capability of 150 nm, and maximum PR thickness of 1.3 um.

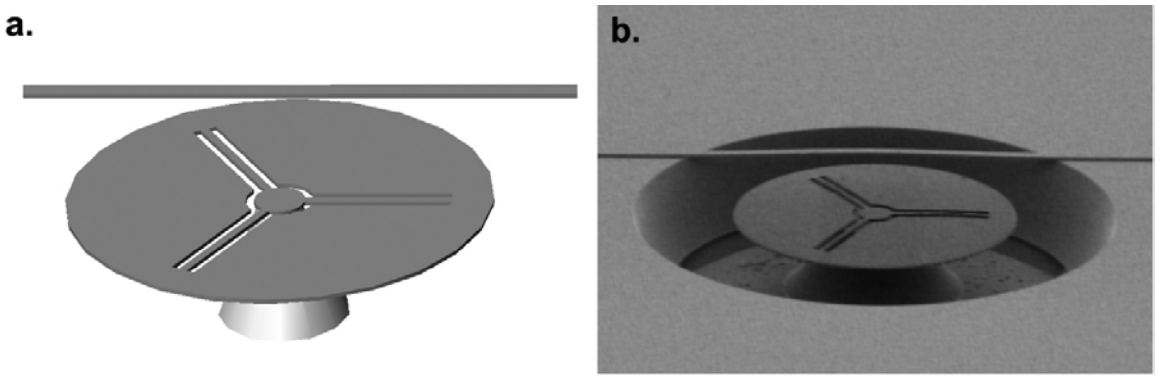

Figure 2.4. a) 3D model of the silicon nitride microring design. b) Fabricated silicon nitride microring.

The fabrication process for the thermally isolated silicon nitride microrings is illustrated in Fig. 2.6a-e). In order for the ring element to be of use, many ring devices must be processed in an array with very high uniformity. The first fabrication attempt was successful in creating the desired geometry by using PR as the masking material for the undercut etch mask shown in Fig. 2.6a–d, but the undercut was non-uniform. In some areas the isotropic oxide undercut step ran along the interface of the PR and undercut the PR at the same time as the microring. To remedy the problem the PR mask was replaced with a hard mask made of polysilicon, which produced very uniform and repeatable structures. A uniform array of completed devices can be seen in Fig. 2.5.

Due to the stresses generated during the high temperature processing; the bus waveguide was significantly deflected in the open region of the undercut. Figure 2.7 shows an interferometer reading of the bus waveguide, with out of plane defection in the open region where fringes can be seen. Deflections of 1.0μm-to-2.0μm were observed.

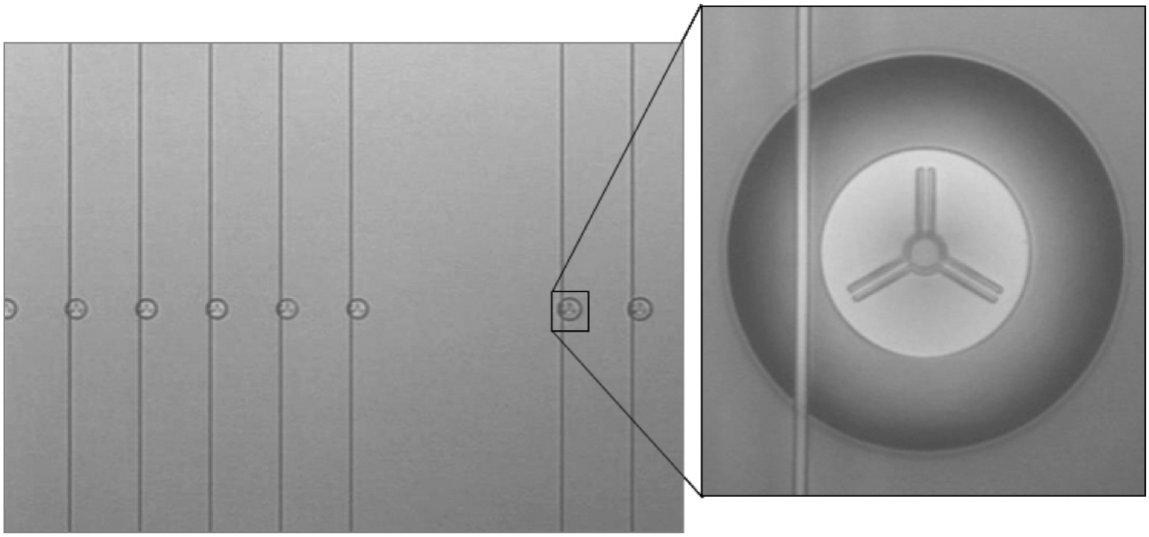

Figure 2.5. Array of uniform microrings demonstrating uniform undercut etch.

This is counter to popular belief that stress in nitride is always tensile, and that even though it is widely accepted that most nitride are deposited in tensile stress, after high temperature annealing, the film has deformed and is compressive when released.

Despite the imperfections of the initial fabrication of these detectors, reasonably high quality factors were observed. The measured resonance of one of the tether microrings is depicted in Fig. 2.8 below where it was found to have a resonant width of ~ 0.1nm corresponding to a quality factor of $Q \sim 15,000$ at a wavelength of $\lambda = 1507$nm. The quality factor was believed to be limited by a design flaw that brought the tether contacts to close to the edge of the resonant microring causing it to interfere with the propagating mode. Evidence of this being due to a design imperfection rather than a fabrication problem is that microdisks (i.e. without tethers) fabricated on the same chip exhibited quality factors $Q > 10^5$.

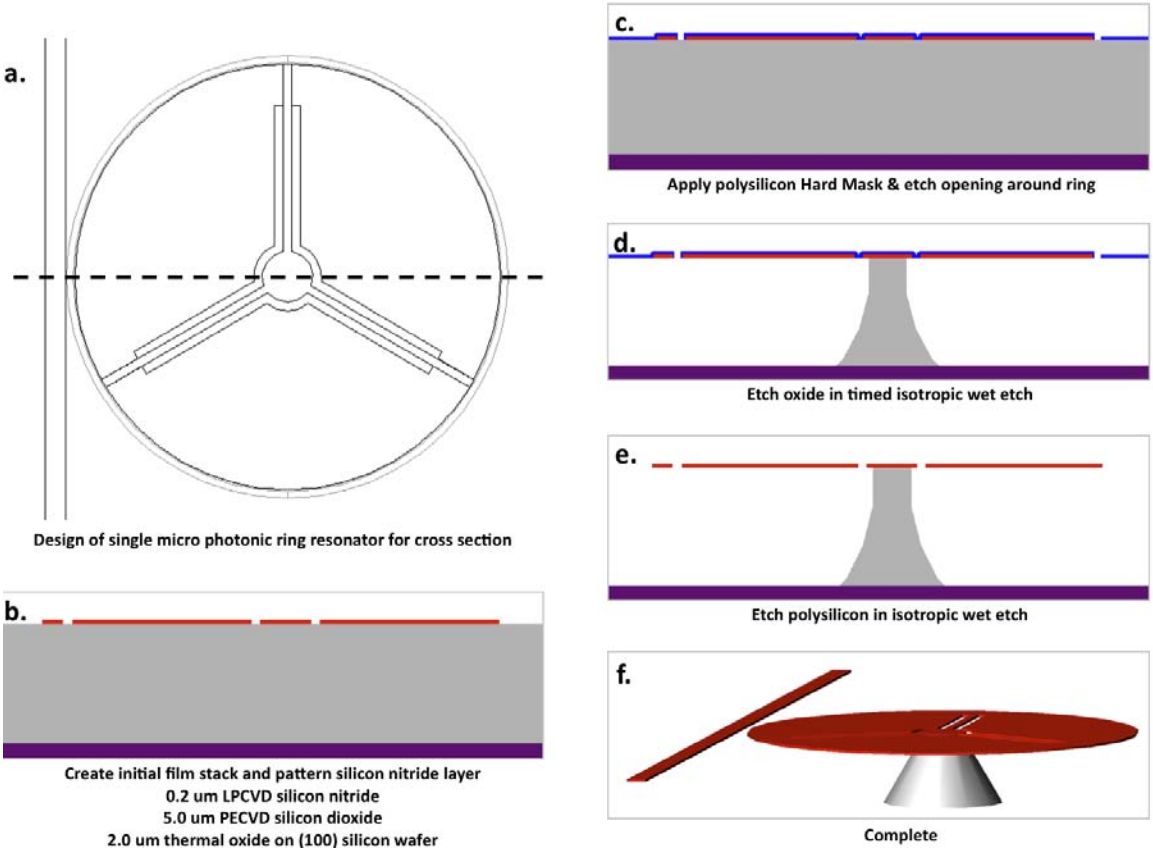

Figure 2.6. Process steps required in fabricating the silicon nitride microring TM-FPA sensor. Two dimensional (2D) renderings were generated with the Sandia 2D Process Visualizer, Version 2.35, generated from the photolithography mask design file drawn in AutoCAD^{TM}.

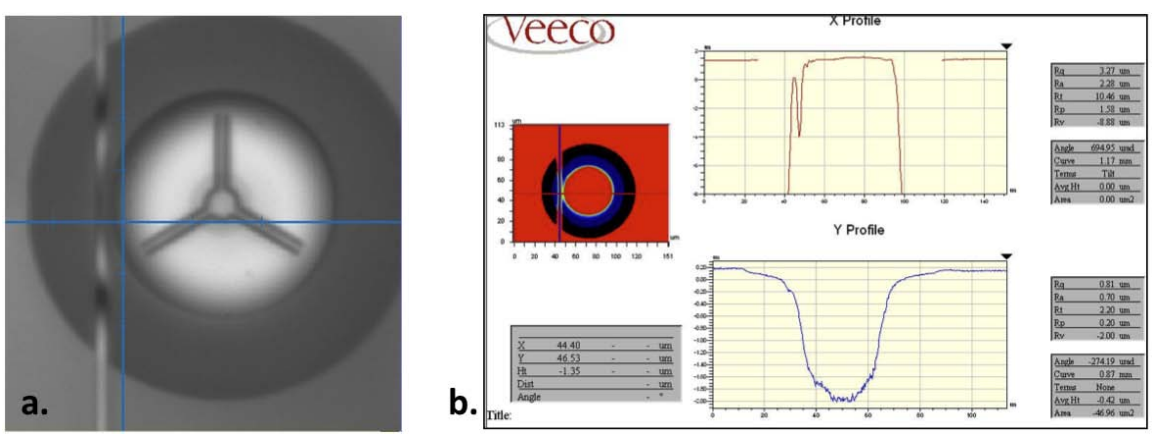

Figure 2.7. Interferometer reading of a nitride waveguide buckling over the open region of the evanescent coupler.

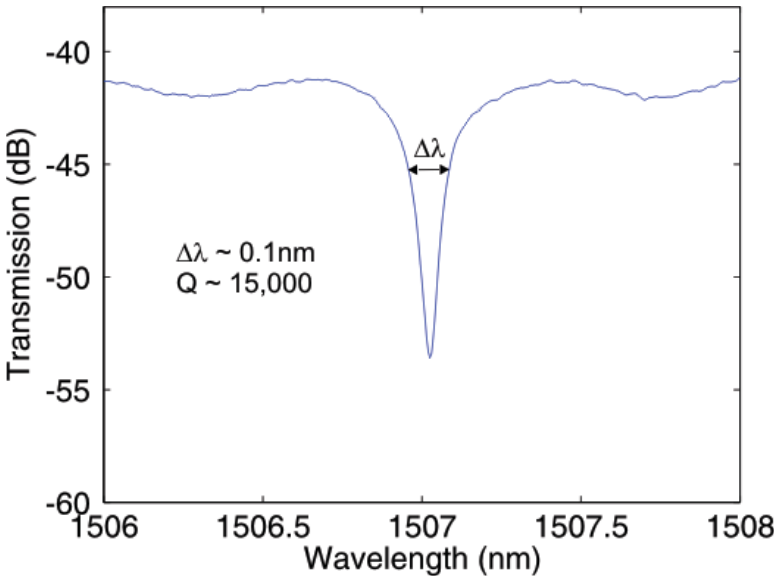

Figure 2.8. Measured resonance of a 20μm tethered silicon nitride microring resonator.

Alternate Silicon Nitride Process

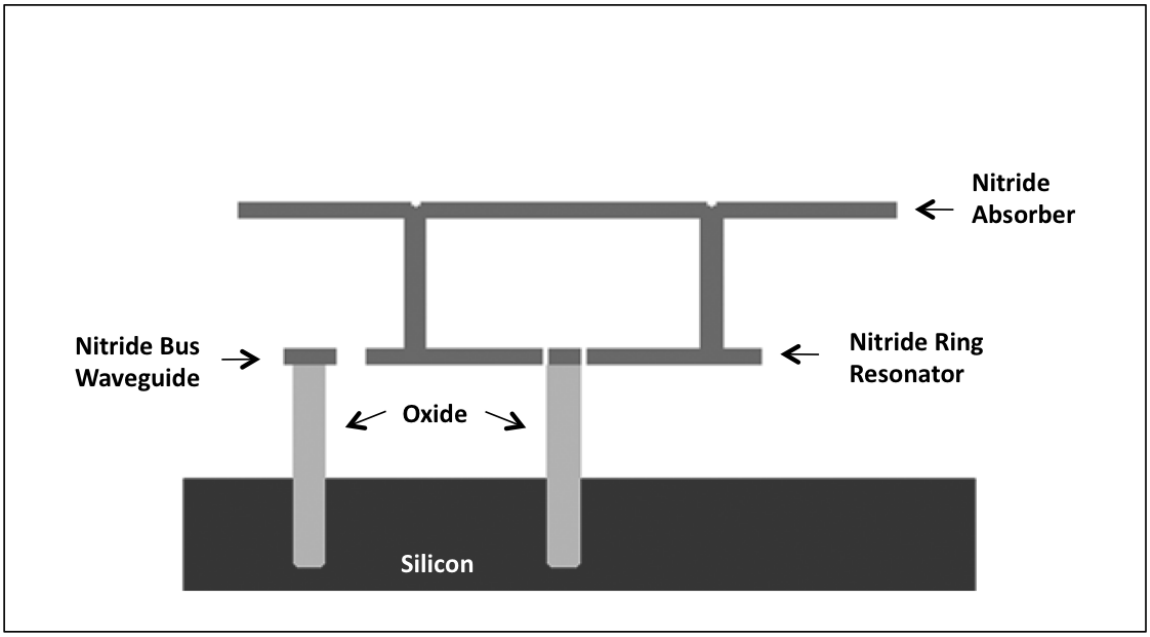

Figure 2.9. 2D Process model representation of a cross section view of the new design using an alternate fabrication process flow.

In the baseline fabrication approach for silicon nitride microphotonic thermal detectors, the detectors were suspended using a timed wet-etch. The wet-etch process is sufficient for single detector demonstrations, but since it exhibits a non-selective etching of the oxide cladding, the bus waveguide is under-etched as well. If many detectors were aligned side-by-side, this approach would lead to a complete lack of support for the bus waveguide. Therefore the baseline approach is not suitable for fabricating imaging arrays. Here, we introduce an alternate fabrication strategy in an attempt to selectively suspend the detector without suspending the bus waveguide. Fig. 2.9 shows a 2D Process Model representation of a cross section view of how the new design would look as fabricated. The nitride ring resonator is tethered to an oxide post in the center of the ring similar to previous designs, and the nitride bus waveguide comes into close proximity to the ring while being supported on the oxide fin. The top layer is a Nitride absorbing layer above the ring resonator which is connected to the outer region of the resonator ring with nitride posts. An outline of the process steps can be seen in Fig. 2.10.

Process induced stress is a significant factor and could cause the oxide fin to buckle laterally if it is not thick enough. Modeling was performed in ANSYS to determine a safe fin width dimension, so the design could be fabricated below the buckling limit. Fig. 2.11 shows the plotted results of the stress analysis.

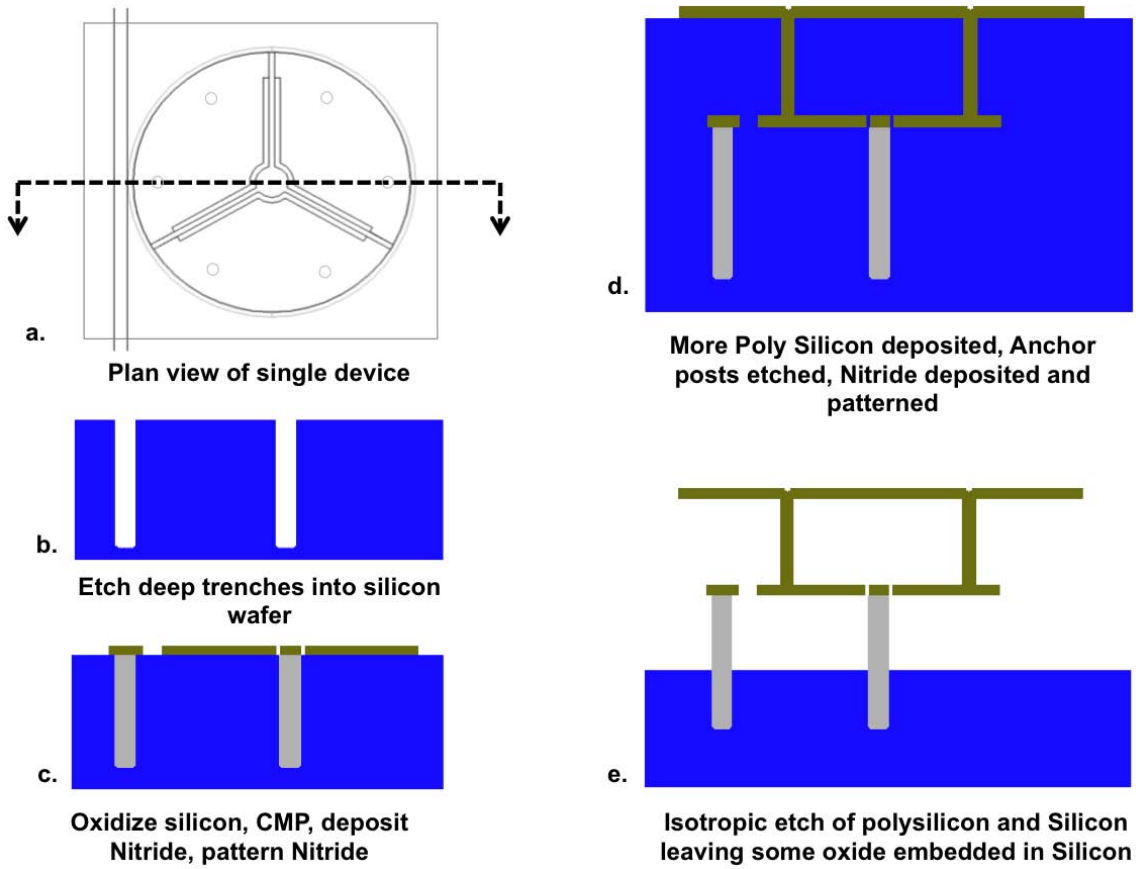

Figure 2.10. Outline of process sequence to fabricate Gen2 TMFPA device.

The stress typically generated in an oxide film attached to silicon and annealed in standard MEMS processes is approximately 300 MPa. The wall thickness of 0.5μm was chosen for this design to insure no buckling would occur. The ANSYS modeling of the stress in the fin structures was successful and no buckling of the fins was observed. The fins were manufactured as intended but several processing and design issues arose for the test design, the details of which will be discussed below. Some of the released devices were diced and the block structures at the end of each waveguide structure proved to be sufficient in protecting the tall fins from being fractured by the saw as can be seen in Fig. 2.12.

While choosing the optimum design dimension for the trenches, one must consider the capability of the tool set. Fig. 2.13 shows the variation of trench depth using the same etch recipe. The etch recipe was created to produce straight sidewalls and maximum depth. As can be seen in the smaller feature, there is less depth and it was determined that structures less than 0.5 um would not survive the silicon etch release etch intact and would fall off the surface. Oxidation thickness was investigated to determine the thickness necessary to cause the sidewalls of the oxide to coalesce, and it was found

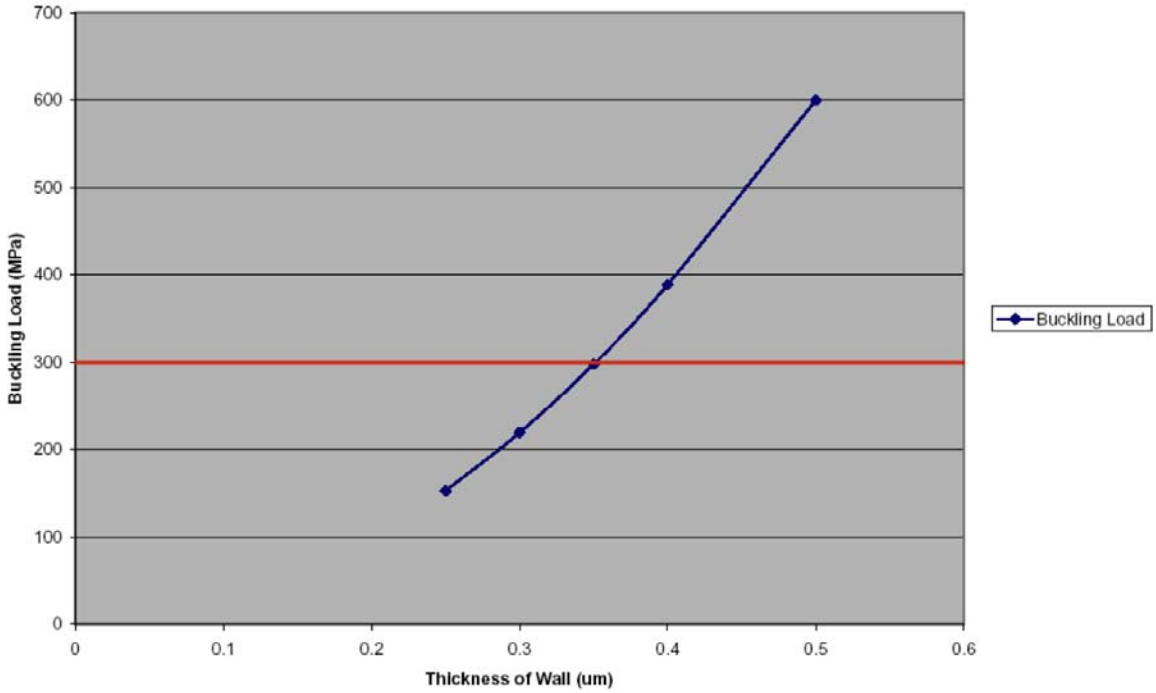

Figure 2.11. Stress analysis of the oxide fin structure showing the buckling load versus fin thickness.

that a heavy oxidation was needed to get good joining of the surfaces. Fig. 2.14 shows the experimental results of several oxidation times / thicknesses. Unfortunately the longer oxidation time caused the flaring effect where the top surface was larger than the intended waveguide design. Furthermore, even the longest oxidation times that were expected to create a dense and continuous oxide, showed lower density regions in the oxide surface that appeared as voids, and were discovered in SEM analysis as can be seen in Fig. 2.15.

High temperature annealing didn't appear to help with the problem. The solution to this problem is to choose a shorter oxidation time to reduce the flaring behavior in the oxidation process, and blanket etch the surface back to create a channel, followed by a High Density Plasma (HDP) of void free dense oxide. An image of the blanket etch strategy can be seen in Fig. 2.17, as well as a flared fin that has been over etched down past the nitride waveguide to remove the flared top edge. A combination of these strategies will most likely be needed to accomplish the desired results.

The CMP process step required after the oxidation of silicon trenches that creates the oxide fin and resonator ring support posts caused a problem on test device structures that had feature sizes larger than 0.5 um. Due to the deep hole left behind after oxidation, it was discovered that the slurry was unable to be cleaned out of features of particular dimensions, and a new mask set was needed in order to eliminate any trench and post features that had openings larger than 0.5 um.

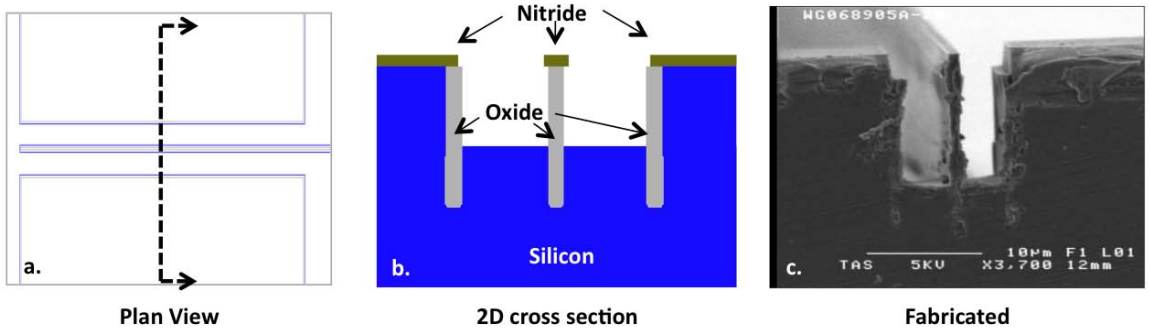

Figure 2.12. Block structures to preserve the waveguide during dicing.

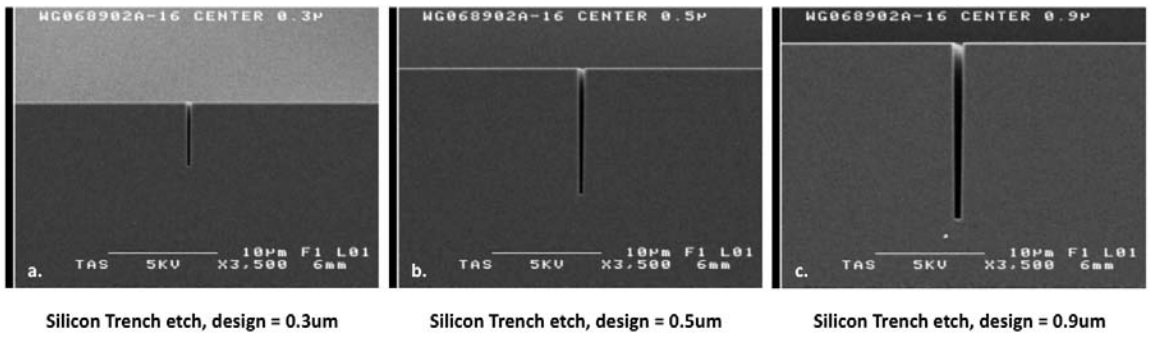

Figure 2.13. Variation of trench depth using the same etch recipe.

It was observed that the smaller fin structures on the test pattern mask did not etch deep enough as seen in Fig. 2.13, to allow for the isotropic silicon etch that is needed at the end of the process to reveal the oxide fins and posts. Also, some of the nitride waveguide features came loose from the top surface of and the narrowest oxide. The smaller fin features would need to be eliminated from future designs in order to eliminate any debris from landing on other devices.

Thinning of the nitride ring resonator during the isotropic Silicon release etch, combined with stress and incomplete release caused the ring structures to become deformed as can be seen in Fig. 2.18, and un-testable.

The fabrication process anticipated the thinning problem by including a sacrificial oxide film on the nitride surfaces. However, the oxide etch rate in the isotropic silicon etch was under estimated and the oxide was depleted leaving the nitride exposed to the etch environment. A simple fix for this problem is to deposit a thicker oxide film on the surface of the nitride before the nitride is patterned. Buckling in Nitride spokes due to the thinning was also observed, an occurrence that was not seen in the previous design. A new spoke design and the addition of etch release holes are shown

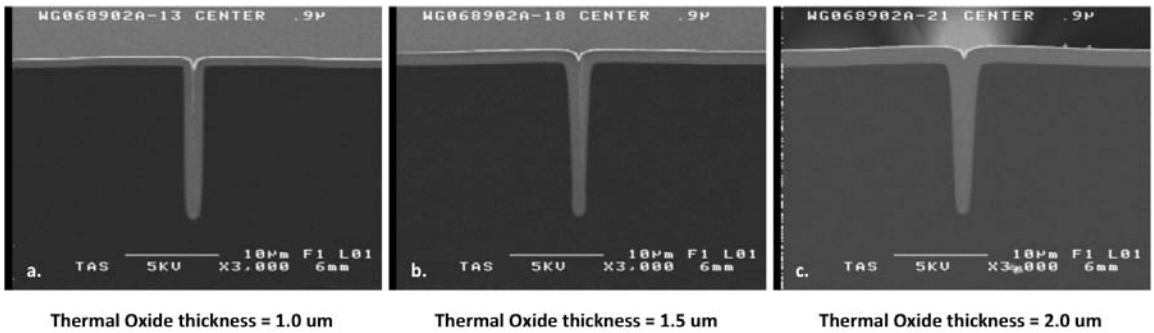

Figure 2.14. Oxidation profiles for various oxidation times / thicknesses in silicon trenches.

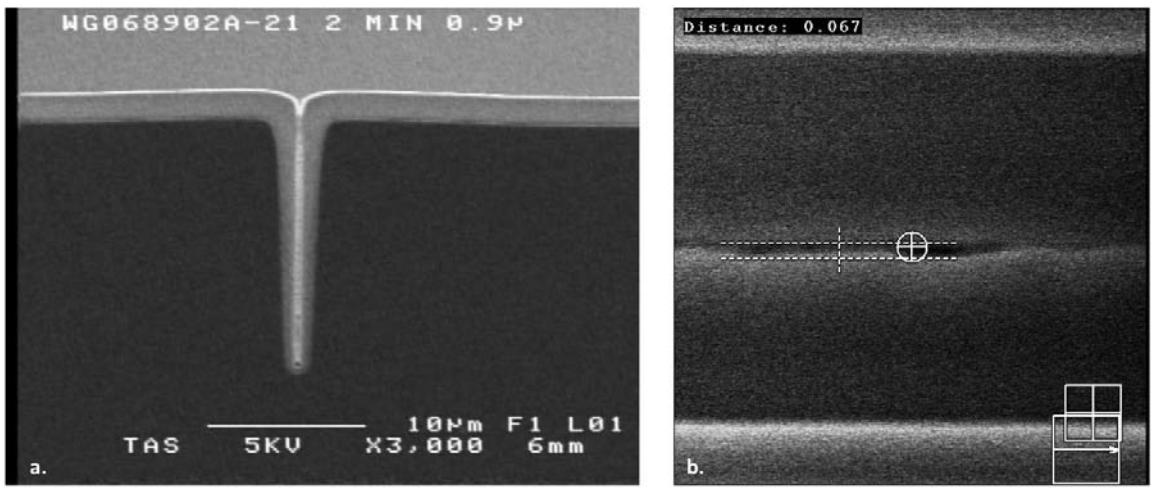

Figure 2.15. Small voids appear in oxide fin structures after subjecting to HF chemistry.

in Fig. 2.18.

Fig. 2.17 shows the un-etched region of silicon under the rings has caused these devices to be non-functional. It is thought that the majority of fabrication and design issues have been identified and mitigation strategies have been implemented or planned out. The results of this fabrication strategy were limited only by available resources. Should a new project with this technology be proposed, the technology development should be relatively straightforward.

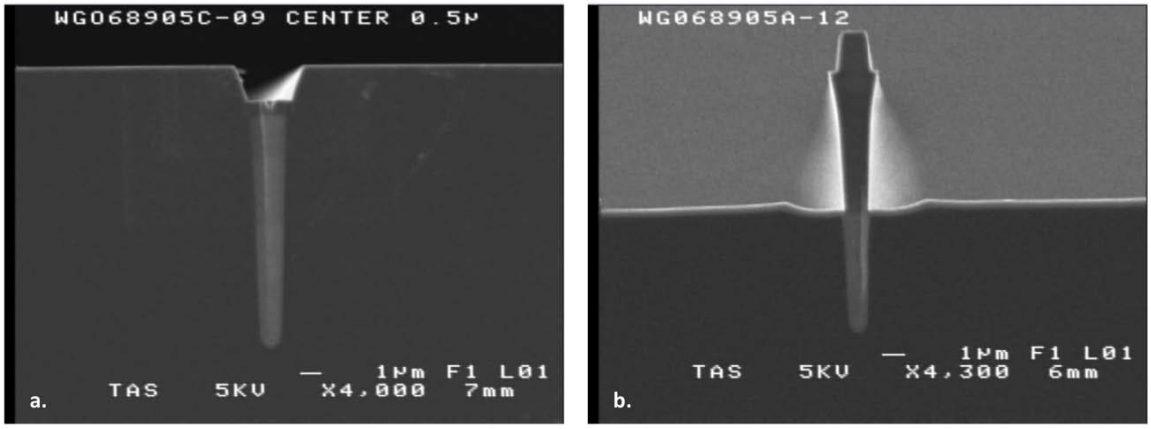

Blanket etched fin in preparation of HDP oxide fill to remove the flare and small voids at oxide to Nitride waveguide interface

Fin with nitride waveguide with the flare edges removed by over etching the nitride

Figure 2.16. Oxide fin fabrication strategies used to mitigate voides at the oxide to nitride interface and flare edge removal.

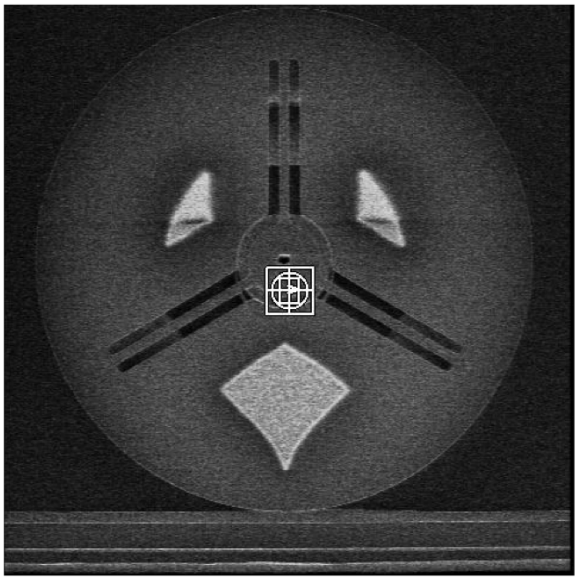

Figure 2.17. Incomplete release of suspended microring-resonator using the as-described alternate silicon nitride fabrication approach.

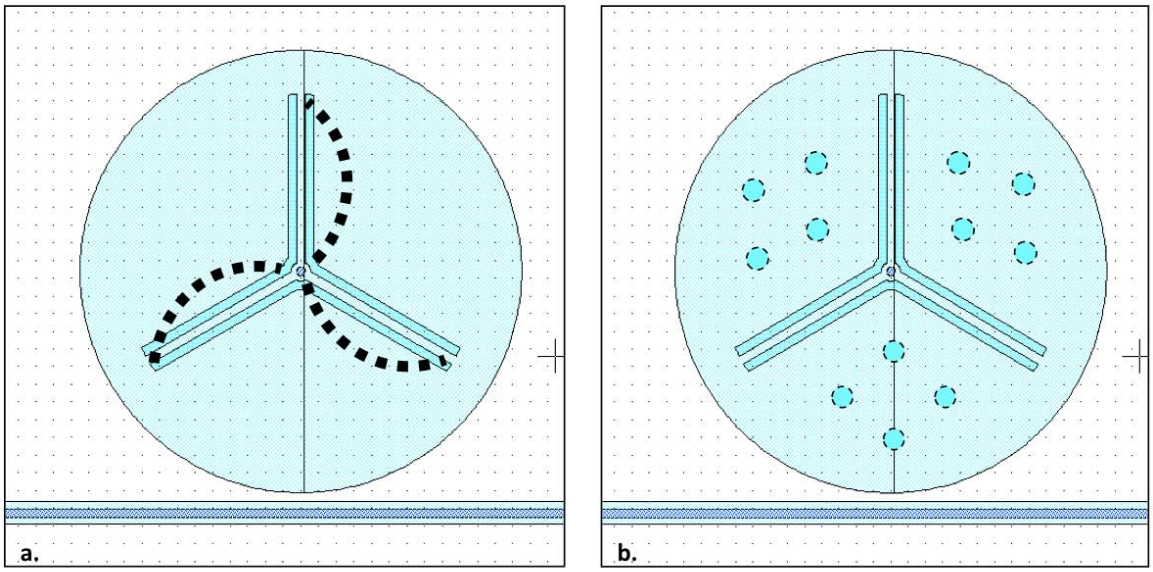

Dashed line shows the concept of a new compliant tether design to eliminate buckling.

Adding release etch holes will insure complete release of the resonator disk.

Figure 2.18. New design concepts to eliminate buckling in the tethers and etch release hole to insure complete release.

Summary

Initial results of our efforts for microphotonic thermal detectors, proved challenging. Given the MEMS-like structure of the detectors, this was expected. Still, we successfully realized single-pixel devices with sufficient quality factor to allow for interrogation of the devices, the results of which are presented in the subsequent chapter. Future efforts in the development of these detectors will need to concentrate on achieving large-scale fabrication of these elements. Certainly, with greater resources, doing so, will be possible.

Chapter 3

Experimental Results

As described in Chapter 2, the silicon nitride pixel depicted in Fig. 2.6 was successfully fabricated in Sandia's silicon (CMOS) fabrication facility using optical lithography. In this section, we describe the experimental apparatus and measurement techniques which were employed to calibrate and measure the sensitivity of the fabricated microphotonic thermal detector.

Measurement Apparatus and Methods

In this section, we discuss the measurement apparatus and the approach that was employed to characterize the sensitivity of the suspended photonic microring cavity as a thermal detector. Through study of the microphotonic thermal detector, we developed the apparatus seen in Fig. 3.1. The microphotonic thermal detector sits within a vacuum chamber which is pumped down to 10^{-5} Torr to improve thermal isolation of the disk from the device substrate– causing the effective thermal resistance of the suspended microring to increase from $\sim 10^{-6}$W/K to $\sim 10^{-8}$W/K. Fiberoptic and electronic feedthroughs allow coupling of 1550nm light into and out of the chip through use of lensed fiber optics which are aligned with remotely operated motorized stages within the vaccum chamber. As will be described further, the optical signals at 1550nm are used to interrogate small changes in the microcavity resonance, which are induced by an incident long-wave infrared reference signal (LWIR). Through development of this apparatus, we used a CO_2 laser, emitting light at 10.6μm, as the reference source. As can be seen in Fig. 3.1, the CO_2 laser is externally electrically modulated as a square-wave. The 10.6μm wavelength beam is attenuated and directed onto the sample through the transparent window of the vacuum chamber, resulting in flood illumination of microphotonic thermal detector. Due to both attenuation and the spatial extent of the beam, small amounts of power (nanowatts) are generally impinging on the microdisk cavity under test.

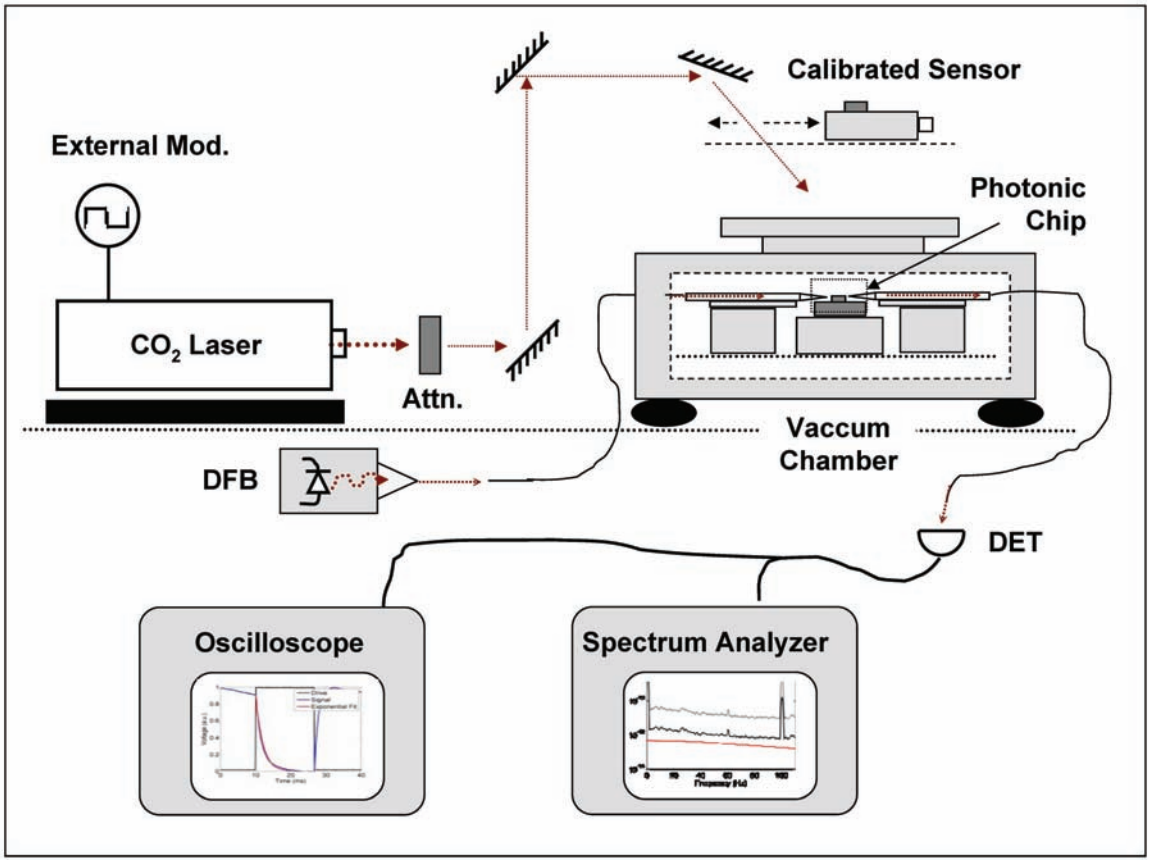

Figure 3.1. Apparatus used for test of thermal responsivity of microphotonic thermal sensor. Near IR Laser light (1550nm) is coupled into and collected from the microcavity within a vaccum chamber while a highly attenuated and modulated Mid IR (CO_2) laser signal diffusely illuminated the device through a transparent chamber window. When the microcavity resonance is properly excited by the 1550nm signal, the 1550nm signal is detected with an InGaAs PIN detector and analyzed with an oscilloscope and/or an RF spectrum analyzer. Calibration of the incident CO_2 laser signal is performed by introducing a calibrated (NIST traceable) pyroelectric detector in the CO_2 beam path.

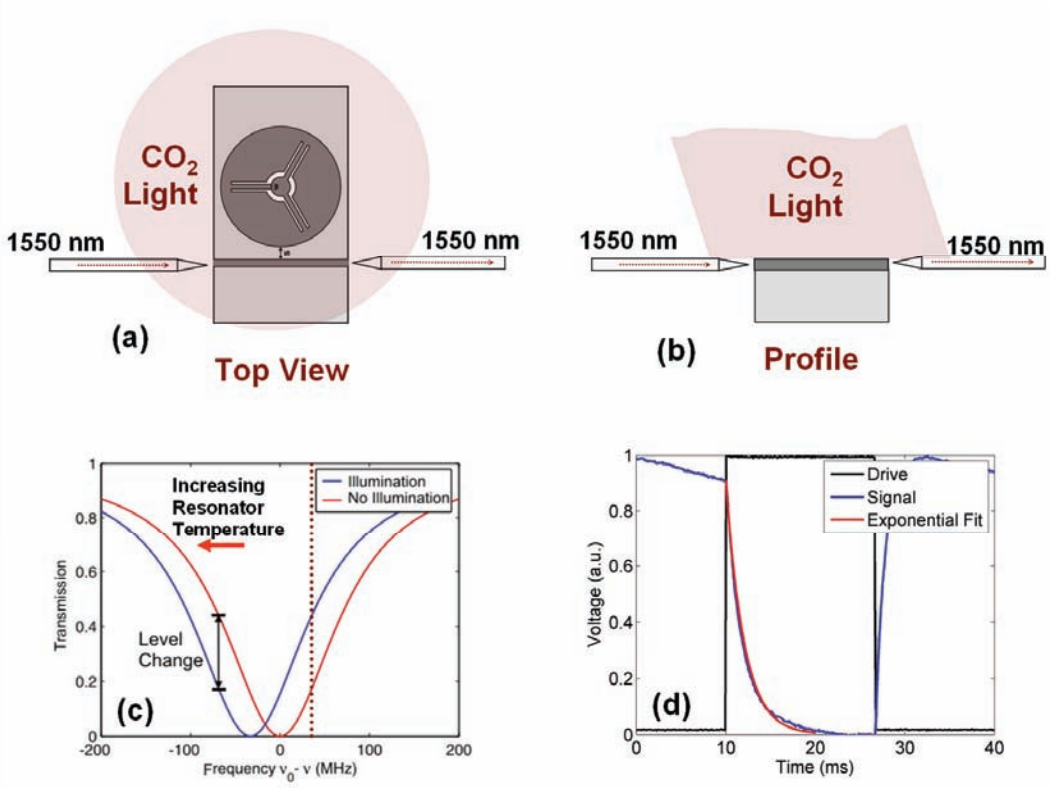

Figure 3.2. (a) and (b) show the basic configuration by which $1550nm$ signals are coupled into and out of the chip using lensed fibers. The manner of flood illumination of the device is shown by the red colored areas. (c) Illustrates the manner in which the cavity resonance shifts when under illumination. The vertical dotted line shows the ideal manner of excitation of the microring for the purpose of detecting the this shift with optimal sensitivity. (d) Shows the resulting measured temporal modulation of the transmitted $1550nm$ signal (blue) which interacts with the ring along with the modulation of the CO_2 laser signal (seen in black).

Since the silicon nitride material absorbs 10.6μm radiation, heating of the microcavity occurs, resuting in cavity frequency shifts, and a time dependent modulation of the 1550nm signal which interacts with the ring. The modulated 1550nm signal is then detected and analyzed in both the time and frequency domains with oscilloscopes and spectrum analyzers, respectively, as depicted in Fig. 3.1.

Accurate determination of the microphotonic thermal detector sensitivity is key to determining its potential technological benefits. To establish detector sensitivity, we must first establish the amount of 10.6μm power incident on the microphotonic thermal detector. To do so, a NIST traceable power calibrated pyroelectric sensor was

inserted into the beam path both inside and outside of the chamber, allowing us to precisely quantify the incident power. The 1-mm diameter pyroeletric sensor provides a calibrated measure of the incident power per unit area which impinges on the sample. With an average power of 1.1mW emanating from a 10Hz modulated CO_2 laser (i.e. measured to be 64mW before final attentuation), the NIST-traceable detector exhibited a peak voltage swing of 7V. The CO_2 was heavily attenuated for two reasons: (1) the CO_2 laser itself exhibits considerable excess noise and (2) the NIST-traceable detector saturates at around 7V. The transfer function of the detector is 8.25×10^4W/V, so the incident average power level was 42μW on the 1-mm aperature. Given that the diameter of the laser beam was several millimeters, the intensity of the beam across a 1-mm aperature can be assumed to be uniform, providing a power-density of 53W/m^2. However, this power level was measured outside the chamber and the transmission through the chamber window was measured separately to be $T_{window} = 0.7$. Further, during operation, the laser power was measured to be 35mW before final attenuation resulting in a combined reduction in the power density to 21W/m^2. Given the diameter of the microphotonic thermal detector is 20μm and the reduced average power incident on the microphotonic thermal detector, $\langle P_{inc} \rangle$, was determined to be $\langle P_{inc} \rangle = 6.6$nW. The external noise performance of the microphotonic thermal detector can be determined directly by taking a spectrum of the received signal. First, however, to calibrate the power level on the spectrum analyzer, the power in the first harmonic of the square-wave must be determined. The Fourier series of a square wave is given by

$$a(t) = \frac{4}{\pi} \sum_{n=1}^{\infty} \frac{1}{n} \sin(2n\pi f t) \tag{3.1}$$

where n is the first harmonic in the square-wave signal. The thermal response of the detector modifies the Fourier series by its frequency response. Thus, the power in the first harmonic is given by

$$P_1 = \frac{\langle P_{inc} \rangle \, |F(\omega_1)|}{\sum_{n=1}^{\infty} \frac{1}{n} \, |F(\omega_n)|} \tag{3.2}$$

and the measured spectrum can be normalized to this peak where $F(\omega)$ is given by

$$F(\omega) = \frac{1}{1 + j\omega \cdot \tau} \tag{3.3}$$

and τ is the detector's thermal time constant. The thermal time constant is readily measured by taking a time domain trace and fitting the decay time of the detector to an exponential. Chopping the CO_2 laser with a 30Hz signal, we fit an exponential to the experimental data in Fig. 3.3, we establish a detector thermal time constant

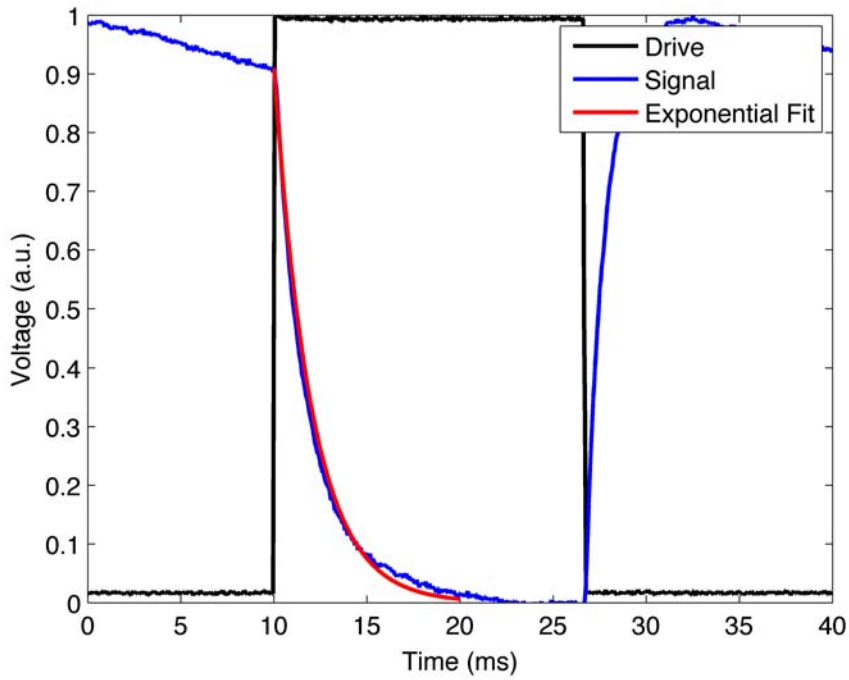

Figure 3.3. Response of the pixel to a 30Hz square-wave modulated CO_2 laser signal incident on the pixel. An exponential fit to the time domain response indicates demonstrates an exponential time constant, $\tau = 2$ms. This rapid response demonstrates applicability to a 240Hz frame-rate where the frame-rate is set to be approximately one over the rise time, i.e. $1/t_r$.

of $\tau = 2$ms. The average power in the first harmonic of the square-wave modulated signal can now be determined from equation (3.2). To get move away from potential close-in noise resulting from fiber vibrations and other sources, we calculate the power for a first harmonic sitting at 100Hz resulting from a 100Hz square wave. Doing so, the power in the first harmonic is found to be 3.5nW.

While we now know the power in the first harmonic of a 100Hz square-wave, a couple of additional steps must still be performed. The spectrum analyzer records the power spectral density of the detected signal. However, in the microphotonic thermal detector, the received power changes the photocurrent in the near-IR detector which in-turn results in a change in voltage at the output of the near-IR detector's transimpedance amplifier. Therefore, the detected CO_2 power is proportional to the near-IR receiver's output voltage. Since the spectrum analyzer squares this voltage to generate a power spectrum, we must take the square-root of the power spectrum to get the true power of our microphotonic thermal detector. Another problem that arises is that while we can take the data with a 1-Hz resolution bandwidth, the square-

root operation effectively widens the resolution bandwidth by a factor of $\sqrt{2}$. This factor must be accounted for to get an accurate reference for the power spectrum. Doing so, we arrive at a 1st harmonic peak with a power level of 2.5nW (with a resolution bandwidth of $\sqrt{2}$Hz or a corresponding 1Hz peak of 3.5nW). The external noise performance of the microphotonic thermal detector is plotted in Fig. 3.4. The external noise performance is not bad, but not exceptional either. However, we did not spend much time designing the absorber prior to fabrication and according to the RCWA results of Chapter 1, we should expect only about 7.5% absorption of the incident radiation, if we assume 20μm diameter, 200nm disks, suspended 10μm above a silicon substrate on 25μm centers. If this were true, the internal noise equivalent power should be $NEP_{internal} \sim 1pW/\sqrt{Hz}$. One caveat here of course is that in the measurement we do not have a periodic array, but rather a single pixel. From a simple ray-tracing picture, a single pixel has a greater fill factor when the normalization is over the area of the detector alone. On the other hand, a single pixel can be expected to absorb less of the incident radiation because it does not benefit from absorption of secondary reflections from adjacent pixels.

Internal Noise Performance

Fortunately, the determination of the internal noise performance of the microphotonic thermal detector does not rely on the RCWA simulations and represents a completely independent analysis from the external noise performance. It does, however, require considerable care in the calibration of the absorbed radiation which is determined from a combination of measured detector parameters. The basic approach involves the following steps: (1) Establish the peak frequency shift under illumination, (2) measure the temperature coefficient of frequency of the detector, (3) convert the peak frequency shift into a measure of peak absorbed power, and (4) using this measure, normalize the absorbed power of the measurement taken in the time and/or frequency domains.

The detector thermal time constant was determined in the previous section by fitting an exponential decay to the time domain response of the detector to a square-wave excitation of the CO_2 laser. The fitted response demonstrated a 2ms thermal time constant. The thermal time constant, τ, is not only an important parameter for detector operation, but also an important parameter for detector characterization as it relates the detector's heat capacity, H, to it's thermal conductance, G.

$$\tau = \frac{H}{G} \tag{3.4}$$

Thermal conductance of a thin film can vary substantially from bulk values due to finite size effects limiting the available phonon-modes. However, the specific heat

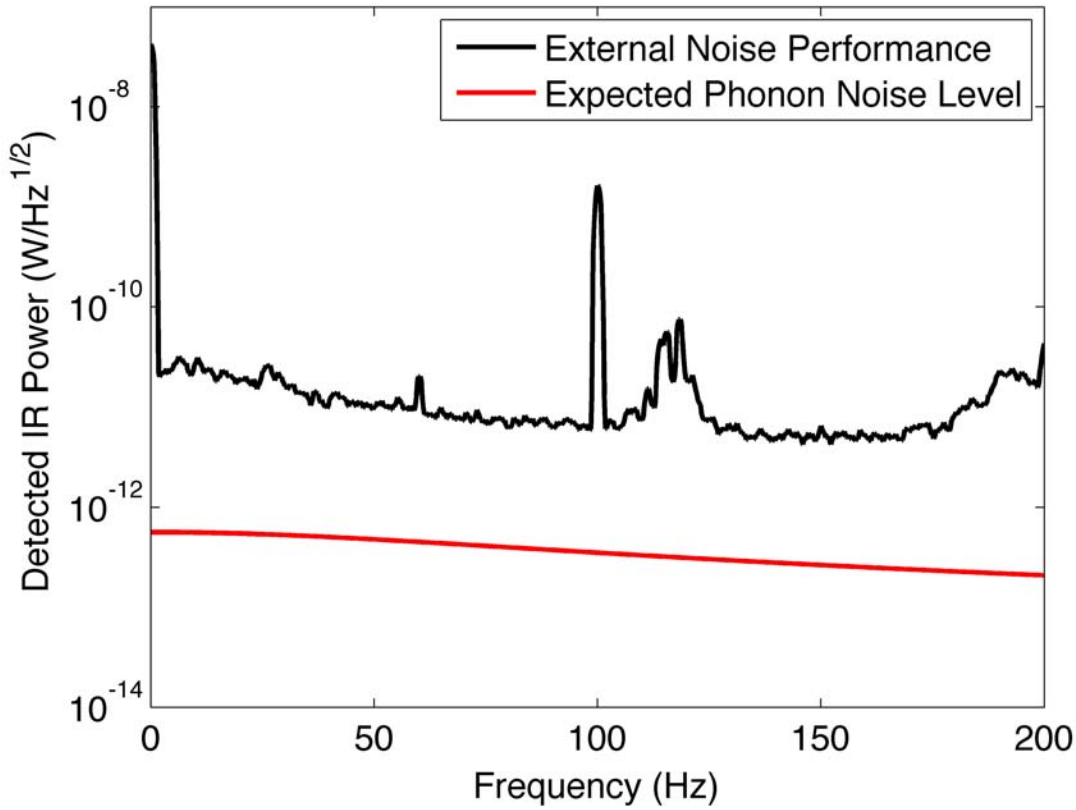

Figure 3.4. The frequency domain response of the pixel to a 100Hz square-wave modulation of the CO_2 laser indicating the external noise performance. the external noise performance is substantially limited by the poor IR absorption in the detector.

does not vary significantly from bulk values. The heat capacity can then be determined from the bulk value $\rho = 3100\text{kg/m}^3$ and the specific heat of the bulk material $c_g = 710\text{J/(kg·K)}$. Doing so, the heat capacity was determined to be $H = 90\text{pJ/K}$ and through (3.4) the thermal conductance of the detector was determined to be $6.6 \times 10^{-8}\text{W/K}$. The spectral density of the thermal photon noise floor can then be predicted from [2], modified by the pixel thermal response $F(\omega)$. That is,

$$NEP_{Phonon}(\omega) = \sqrt{4k_B GT} \cdot |F(\omega)\,|. \tag{3.5}$$

Further, by measuring the thermo-optic response of the suspended microring-resonator with temperature, the power absorbed by the detector can be determined. The peak temperature change for a given amount of incident power is determined by measuring the peak change in power when sitting on a 3dB-point of a resonance. The slope of the resonance at the 3dB-point is equal to $1/\Delta f_{FWHM}$ where$\Delta\ f_{FWHM}$ is the full width

half maximum bandwidth of the resonance. If we multiply the change in transmission by the inverse of the slope of the resonance, we arrive at the frequency shift of the resonance,$\Delta\ f_{shift} = |\Delta t|^2 \cdot \Delta f_{FWHM}$. The temperature change is therefore simply $\Delta T = \frac{dT}{df}\Delta f_{shift}$. With the heat capacity known from the thermal time constant, the peak absorbed power can then be determined simply from $P_{abs} = \Delta T \cdot G$ and the average power of absorbed is simplg $< P_{abs} >= P_{abs}/2$, as can be shown through simple integration of the modified square-wave response. For our resonance, sitting at $\lambda = 1557$nm, the resonance width was measured to be 0.12nm. Converting to the frequency domain, the resonance width measures$\Delta\ f = 15$GHz wide. Additionally, the thermo-optic coefficient of the resonator was measured to be $\frac{df}{dT} = 1.8$GHz while the peak change in transmission was measured to be $|\Delta t|^2 = 0.1$. The corresponding shifts in frequency and temperature are therefore$\Delta\ f_{shift} = 1.5$GHz and $\Delta T = 0.82$K. The peak power absorbed by the detector prior to final attenuation was therefore 55nW. Post attenuation, the peak power at the detector is therefore $P_{abs} = 1$nW and the average power absorbed by the detector $< P_{abs} >= 0.5$nW. Finally, the power absorbed in the first harmonic is determined in the same manner as for the external case described previously and the result is plotted in Fig. 3.5.

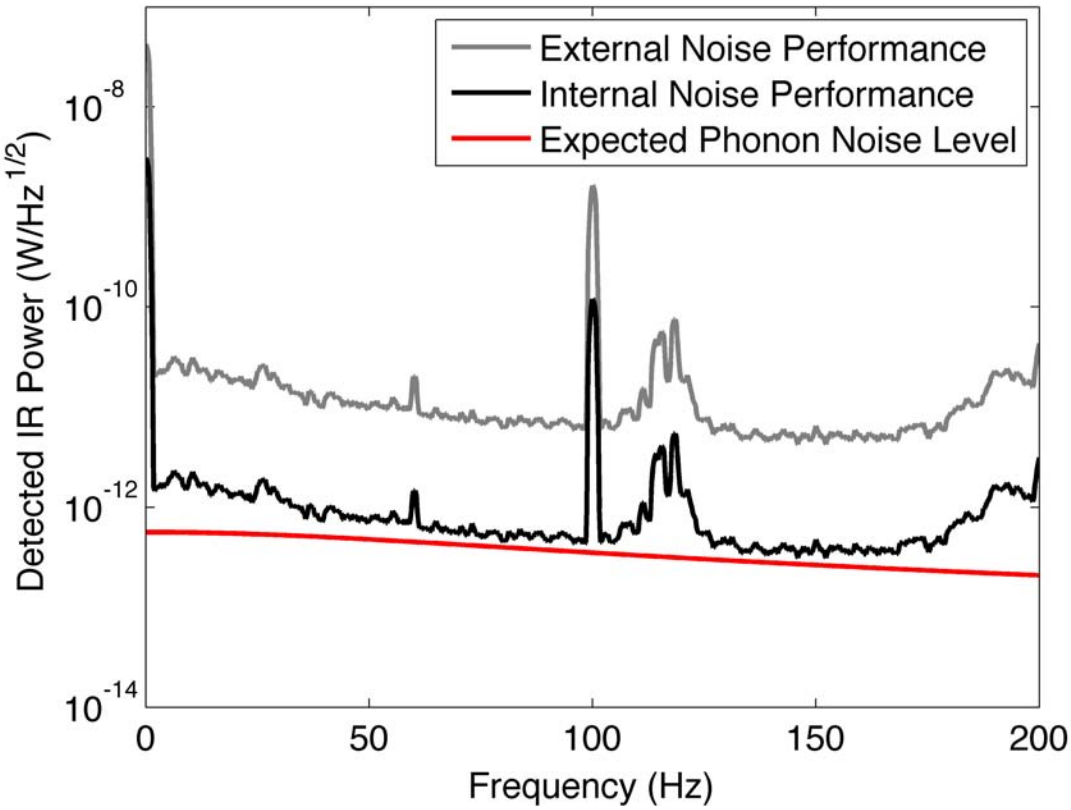

Figure 3.5. The frequency domain response of the pixel to a 100Hz square-wave modulation of the CO_2 laser. The internal noise performance of the detector demonstrates near phonon-noise limited performance.

As can be seen from the Figure, the internal noise performance closely approaches the anticipated thermal phonon noise floor. There is some excess noise close to DC which is likely a result of fiber vibrations and there are 60Hz harmonics likely due to imperfect electrical isolation, but otherwise the result very closely reaches follows the anticipated thermal noise floor. Interestingly, a comparison of external and internal results yields an absorption coefficient for the ring of 7.3% which is in close agreement with the RCWA analysis, supporting our conclusions.

Already we have demonstrated viability of device fabrication with the successful demonstration of a 20μm pixel, and a scalable readout technique. Further, to date, we have achieved internal noise performance ($\text{NEP}_{Internal} < 1pW/\sqrt{Hz}$) in a 20$\mu$m pixel thereby exceeding the noise performance of the best microbolometers while simultaneously demonstrating a thermal time constant (τ = 2ms) that is five times faster. In all, this results in an internal detectivity of $D^*_{internal} = 2 \times 10^9 \text{cm}\cdot\sqrt{Hz}/\text{W}$, while roughly a factor of four better than the best uncooled commercial microbolometers, future demonstrations should enable another order of magnitude in sensitivity. A comparison of the detectivities of high temperature detector technologies is provided in Fig. 3.6. While much work remains to achieve the level of maturity required for a deployable technology, already, microphotonic thermal detection has demonstrated considerable potential.

Summary

Considerable effort was placed into the characterization of the first microphotonic thermal detectors. Using independent techniques the external and internal noise performance of the detector was probed. The experiments and subsequent analysis indicates that even with this crude experimental setup internal noise performance approaches the thermal noise floor of the detector. Moreover, the independent external and internal techniques provide close agreement, confirming these impressive results. Further, based on the RCWA analysis from Chapter 1, a clear path exists for greatly enhancing the external noise performance in the detector. Future efforts will need to be placed on reducing the detector's thermal conductance, improving the resonator-Q, and enhancing the detector's absorption.

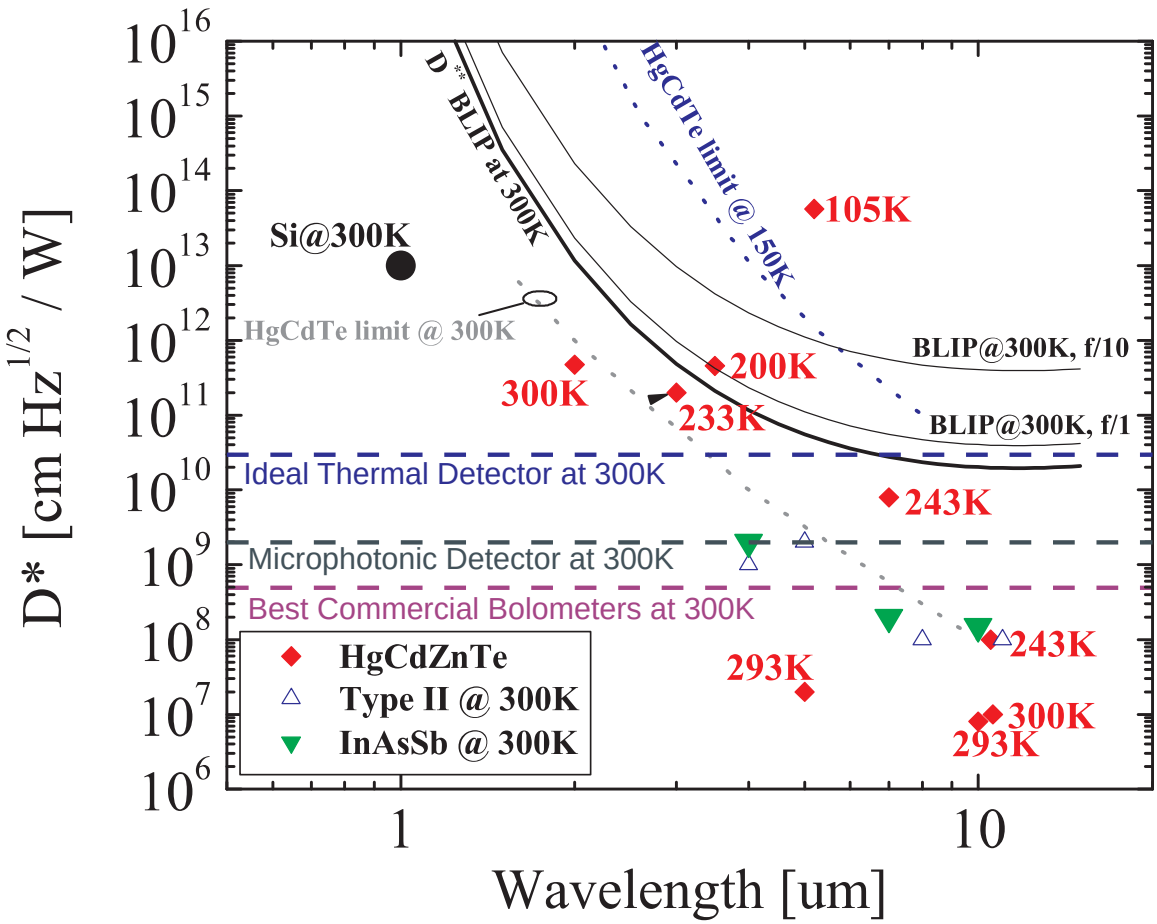

Figure 3.6. Comparison of detectivities of various high temperature infrared detectors. The internal noise performance of the first microphotonic thermal detector exceeds the external noise performance of the best commercial bolometers. Considering the substantial advantage bolometers hold in development time / effort, this result is significant.

Chapter 4

High resolution scalable readout technique for resonant optical sensors

We describe and demonstrate a readout technique for resonant optical sensors by measuring the frequency change of a swept microwave signal to provide a well controlled frequency offset from an optical carrier. The technique has the advantage of being scalable to readout many (millions) of optical resonators and is not only directly applicable to microphotonic thermal imaging, but also to a wide variety of optical sensing techniques. Experimentally, we demonstrate relative optical frequency measurements with a standard deviation of ~ 1 part in 10^{10} that satisfies the requirements for frequency shift measurements in many optical resonant sensors.

Introduction

Optical resonant sensors have been proposed and demonstrated for a variety of applications, among them rotation [9], infrared [1] , bio-chemical [10], and mechanical strain [11] sensing. The degree of frequency shift required to achieve the desired resolution varies per application from ~ 1 part in 10^{14} in rotational sensing for 1 degree per hour rotation rates to ~ 1 part in 10^6 in strain sensing to achieve 1 ue strain measurement. For course sensing applications, optical techniques using tunable lasers and tunable filters provide enough resolution and these interrogators are readily available in the marketplace with resolutions of about 1 part in 10^6. More sensitive effects like rotation or infrared sensing require the development of new techniques in optical sensing to achieve the desired resolutions of 10^{10} to 10^{14}. Of course, it is important that these techniques will have small size, weight, power, and cost.

In this Chapter we describe a technique for measuring the frequency shift of optical resonators in response to an external stimulus. The technique uses a microwave swept signal in conjunction with an optical modulator, filter, and frequency-locked optical source to provide a high resolution readout technique. By sweeping the microwave signal across a wide bandwidth, many resonators can be interrogated by a single

modulated optical signal. By using wavelength division multiplexing, the readout technique can be extended to interrogate millions of resonators, for example in a two dimensional thermal microphotonic focal plane array [1]. Experimentally, we have achieved frequency measurement resolution and repeatability of ~ 1 part in 10^{10} using this technique.

Description of the Basic Technique

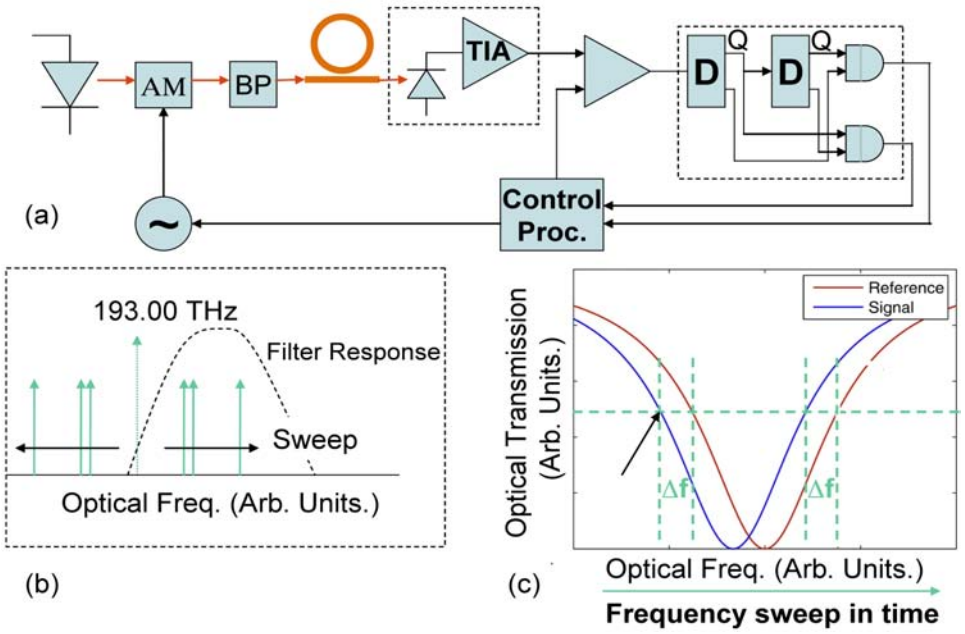

Figure 4.1. (a) Block diagram of the basic readout technique. (b) Spectrum of the modulated optical signal and the optical filter to select one sideband (c) Spectrum of a resonant sensor showing the shift from the applied stimulus relative to the reference position. The readout technique must measure Δf.

Our interrogation starts with a continuous wave (CW) laser as shown in Fig. 4.1. The laser optical frequency, f_c, in this example is 193 THz ($\sim$1550 nm). We modulate the laser using an optical amplitude modulator with a radio frequency (RF) or microwave sine wave that is swept from one frequency to another in a linear fashion with time. As an example, consider the RF modulated signal, f_m, varying from 9 GHz to 11 GHz. After modulation, the optical spectra contains three sets of signals, one at a frequencies f_c-f_m, a signal at the center frequency of f_c, and a set of signals at frequencies $f_m + f_c$ as shown in Fig. 4.1b. If we insert a fairly narrowband optical filter in the signal path after the modulator, we can pass frequencies to the right of the carrier, and reject the carrier and frequencies to the left of the carrier. For

a band-pass filter, the bandwidth of the filter must be wider than the sweep width of the RF generator (2 GHz in our example), but must have high attenuation over a bandwidth of twice the lowest frequency (18 GHz), assuming the modulator gives good carrier suppression. In our example, the optical signal after the filter varies from 193.009 THz to 193.011 THz.

Let's assume that the resonant sensor has an inverse Lorentzian shape as shown in 4.1c and that the initial response of the resonator has a center frequency in the center of the sweep range of 193.010 THz with a 20 MHz FWHM, which are approximately the characteristics in our experimental resonator described later. As the signal sweeps with the range given above, an amplitude detector will be able to measure the frequency (wavelength) response of the resonator. So, in our example, let's assume that when illuminated by infrared radiation, the resonator response shifts so that the center frequency is now shifted by 2 MHz to the left to 193.009998 THz with the FWHM unchanged. In 4.1c,Δf illustrates this shift that we must measure.

Measuring such a small frequency shift relative to the center frequency requires the laser to be frequency-locked to a resonator on the same chip so the laser itself doesn't drift and to compensate for common or background variations of the resonators. Experimentally, we used the well-known Pound-Drever-Hall technique [12, 13, 14, 15] to frequency lock the laser to our experimental resonator.

As the optical signal is swept across its frequency range, we can compare before (or reference resonator) and after amplitude responses to calculate the shift in resonances. However, instead of measuring a change in amplitude at a fixed frequency to infer the frequency shift, we developed a technique to measure the shift directly with a detector followed by a comparator as shown in Fig. 4.1a. The advantage of this approach compared to many others is that analog to digital converters (ADCs) are not required, although a comparator can be thought of as a 1 bit ADC. A reference signal is incident on the other side of the comparator. The value of that reference signal is not critical, but values of 1/10 to 1/2 of the difference between the peak and minimum amplitudes are reasonable. We used a 40% threshold in our experiment.

The center frequency of the resonator can be accurately determined by averaging the frequency at which the downward sloping response crosses the threshold with the frequency at which the upward sloping response crosses the threshold. The precise measurement of those points will be difficult in the presence of noise, because this noise will cause there to be multiple thresholds for both the downward and upward transition. These transition crossings may be averaged independently to arrive at a more accurate and repeatable value for each transition crossing as illustrated in Fig. 4.5.

A simple circuit to detect these transitions is shown in Fig. 4.1a. The signal from the comparator is latched into a pair of sequential D-type flip-flops. At any point in time, the current bit is stored in the first flip-flop and the previous bit is stored in the second flip flop. A bit signifies whether the signal is greater than the reference

(logic 1) or less than the reference (logic 0). Therefore, if we route the Q output from the second flip-flop with the Q-bar output of the first flip-flop (an inverter can be added if there is no Q-bar output) into an AND gate, the output from the AND gate will be high only when the previous bit is a logic 1 and the current bit is a logic 0 which is indicative of the downward slope crossing the threshold. Similarly, if we route the Q-output from the first flip-flop and the Q-bar output from the second flip-flop to a second AND gate, the output from the second AND gate will indicate a threshold crossing on the upward slope. A field programmable gate array (FPGA), digital signal processor (DSP) or microcontroller can do the calculations. It can also incorporate the logic described above.

Now, if we perform this technique for the device in both the initial and final state, and subtract the initial (or reference) center frequency from the final (or device under test) center frequency, this will give the frequency shift, which in turn, gives us a measure of the stimulus strength (infrared radiation in this example).

Extending the technique to multiple resonant detectors

The technique can be applied to interrogate more than one resonator. In Fig. 4.2, the device to be interrogated consists of a series of resonators in a row, each with a slightly different center frequency. The combined response of all the resonators is a series of inverted peaks as shown in Fig 4.2. Each of these might shift independently in response to incoming infrared radiation, for example. If we consider the resonators as having resonances 50 MHz apart, then the RF sweep of 2 GHz in our example can interrogate the response of 40 resonators, and a sweep range of 5 GHz can sweep out 100 resonators. Of course, it is important that the spacing of the resonator be less than the dynamic range of the shift caused by the applied stimulus.

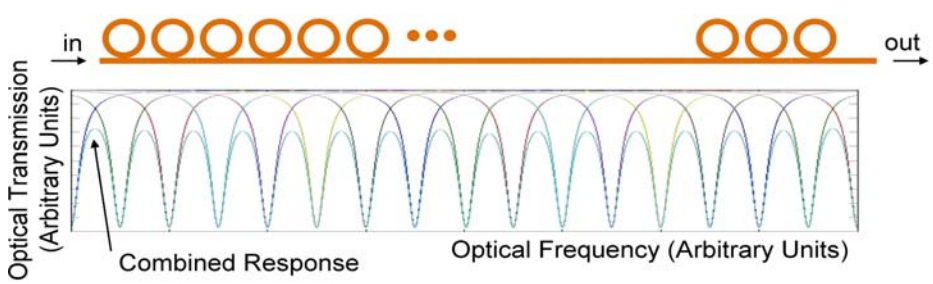

Figure 4.2. Frequency response of many resonators in series. A wideband swept RF signal can be used to readout the positions of all the resonant nulls in one sweep.

Using wavelength division multiplexing in conjunction with this RF swept approach

allows scaling toward 10,000 resonators. There are many ways to consider generating multiple laser lines each with a swept RF signal applied to it. The one with the least number of components is shown in Fig. 4.3. Consider 50 lasers each with an optical frequency separated by 50 GHz, with a lowest frequency of 192 THz (1562.5 nm) and a highest frequency of 194.5 THz (1542.4 nm). A DWDM multiplexer combines the laser signals.

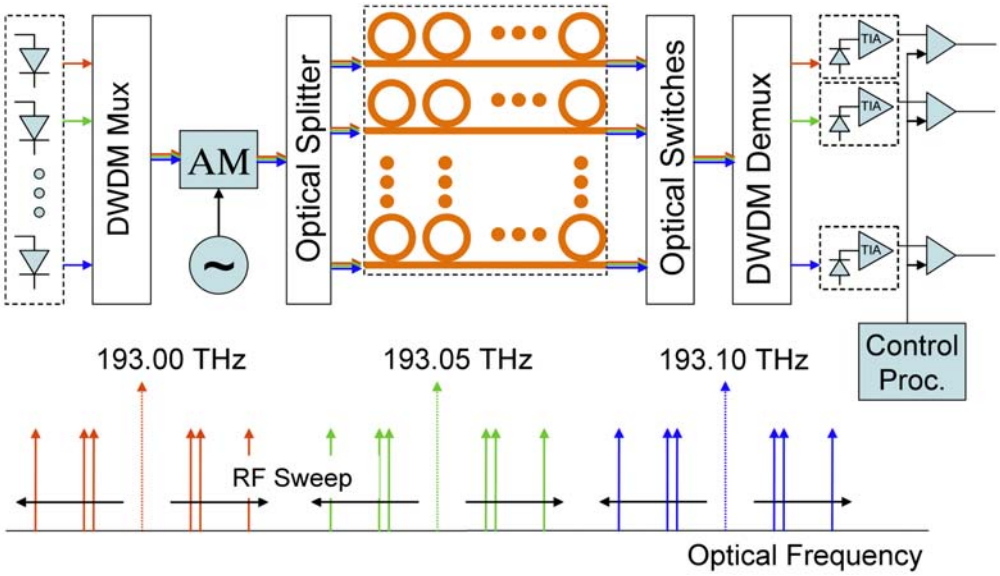

Figure 4.3. Extension of the technique using WDM and parallelism to readout a large array of resonant sensors and the spectrum of the WDM/RF swept readout signal.

A common modulator can be used to generate the spectrum, partially shown in Fig. 4.3 that utilizes both the upper and lower sidebands to generate 100 simultaneously sweeping frequency bands. It is important that the modulator have very low harmonic generation or there will be harmonic frequencies generated in the modulation of one laser that overlap with the fundamental desired frequencies generated by modulating one of the other lasers. If a linear modulator with low harmonic generation is not available, groups of modulated lasers can be interleaved in frequencies and at the limit, each laser can have its own modulator and filter to make sure there are no harmonics in the desired modulated frequencies of another laser.

By using simple splitting techniques and an optical switch (or alternatively parallel versions of the readout circuitry on the right of the optical switch shown in Fig. 4.3) it should be possible to interrogate many rows in parallel. If there are 10k rows (40 dB loss), then it could be feasible interrogate to 100 million resonators.

Experimental Setup and Results.

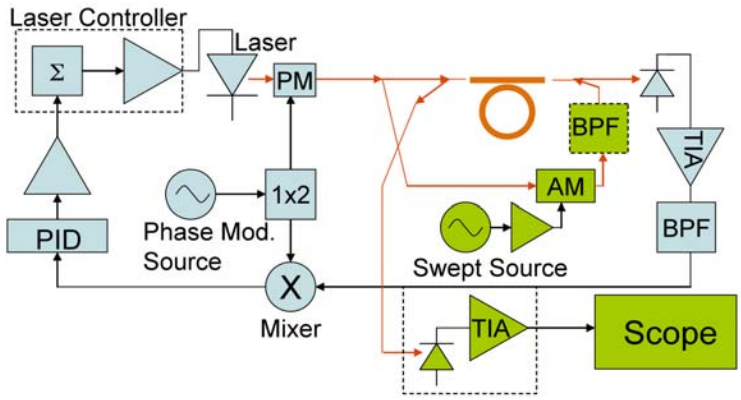

Figure 4.4. Block diagram of the experimental setup used to measure the repeatability of the frequency measurement capability

A block diagram of the basic setup is shown in Fig. 4.4. In our experiments, we used a single large resonator for both the reference and measurement, propagating the reference signal in the clockwise direction and the measurement signal in the counter-propagating direction. The resonator itself was a silica waveguide ring-resonator on glass. The diameter of the ring was $\sim$ 2.5 cm, the free spectral range was $\sim$ 2.6 GHz, and the FWHM was $\sim$ 25 MHz, for a Q of $\sim$ 8 x 10^6 and a Finesse of $\sim$ 100. In our experiment, we used a standard DFB laser with optical frequency of 193.5 THz (1550.39 nm) with an estimated linewidth of $\sim$ 1 MHz. Our reference laser was locked to the clockwise propagating direction of the resonator using the Pound-Drever-Hall (PDH) technique [12, 13, 14, 15]. The components required for the frequency-locking subsection are shown in blue. In the PDH technique, phase modulation (in our case at 197.5 MHz) is applied (in our case with an integrated optical phase modulator) to the signal before it enters the resonator. The combination of the resonator and the detector act as a phase detector, giving a current output from the photodiode, for small frequency deviations, that is proportional to the deviation of the laser frequency from the resonator center frequency in Amperes/Hz. This signal is amplified, filtered, mixed to baseband, and further amplified with a proportional-integral-differential (PID) controller and routed to the current modulation input of the laser diode controller. For a small change in current, the laser frequency will change (from heating and from carrier injection), and the amplitude will be fairly constant. The PDH technique can give a linewidth reduction compared to the original laser. However in our case, limitations in the frequency response of the PID controller, laser modulation function, and possibly additional noise in our system prevented us from seeing any improvement in linewidth compared to the un-locked laser.

A digital synthesizer was used to provide the swept RF signal that was routed to the input of an amplitude modulator that was used to create the swept signals on

either side of the carrier. These signals were supplied to the resonator in the counter-clockwise direction. The DC bias on the amplitude modulator was adjusted so that the carrier was suppressed by observing the signal on an optical spectrum analyzer. The carrier suppression was measured to be $\sim$ 23 dB. We operated the swept RF source three free-spectral ranges away from the carrier at $\sim$ 7.7 GHz. It is difficult to obtain a commercial tunable optical filter with less bandwidth than that. In our experiments, we did not actually use the filter. If the upper sideband is 3 free-spectral ranges above the carrier, then the lower sideband is 3 free spectral ranges below the carrier. Thus when swept through the resonance, both sidebands sweep through together. However, a shift in the measured resonance relative to the reference will provide an asymmetric shift relative to the swept signal, so the filter should be present to measure the shift in response to an external stimulus.

We used an oscilloscope and Matlab post processing to replace the circuit diagram in Fig. 4.1. The traces and calculations are shown in Fig. 4.5. Using the technique described in the first section to average transitions, the standard deviation of the center frequency measurement was measured to be only 11 kHz, with no oscilloscope function averaging on the oscilloscope data. This corresponds to better than 1 part in 10^{10} in frequency measurement. In a thermal microphotonic sensor, this corresponds to measuring a temperature change of approximately 10μK.

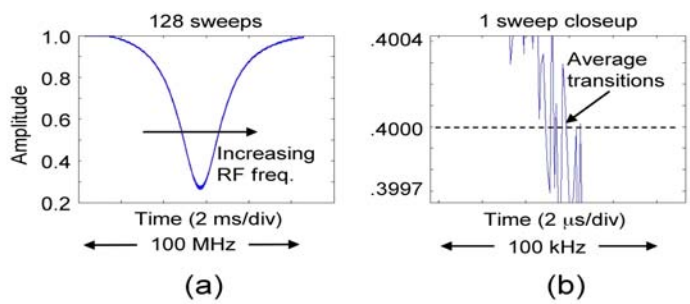

Number of averages = 1, Number of trials = 64
Threshold Mean = 37259.572 kHz, Std. Dev = 11.734 kHz,
Max = 37284.250 kHz, Min = 37226.800 kHz

Figure 4.5. Traces from 64 sweep showing overlay on a wide-sweep (100 MHz) and a close up of a narrow sweep (100 kHz). Below the figures are shown the output data from the calculation showing a standard deviation of the measurement of only 11.7 kHz in the center frequency measurement. Number of averages = 1, Number of trials = 64 Threshold Mean = 37259.572 kHz, Std. Dev = 11.734 kHz, Max = 37284.250 kHz, Min = 37226.800 kHz

Summary

We describe and demonstrate a scalable readout technique for measuring the frequency shift of optical resonant sensors. While we have not demonstrated the response of the device to an external stimulus, the uniformity of the static frequency measurement looks promising for a variety of applications. Future work will include demonstrating array sensing and removing sources of error to further improve the frequency resolution and accuracy.

References

[1] M. R. Watts, M. J. Shaw, and G. N. Nielson, "Optical resonators: Microphotonic thermal imaging," Nature Photonics, **1**, 632-634 (2007).

[2] J. C. Mather, "Bolometer noise: nonequilibrium theory," Applied Optics, **21**, 1125-1129 (1982).

[3] J.W. Gibbs, "Elementary Principles in Statistical Mechanics," Yale Univ. Press, New Haven, (1902).

[4] J. B. Johnson, "Thermal Agitation of Electricity in Conductors",Phys. Rev. 32, pp. 97-109 (1928)

[5] M. R. Watts et al., Thermal Microphotonic Focal Plane Array (TM-FPA) for High Sensitivity Room Temperature Thermal Imaging, Conference on Lasers and Electro-Optics (CLEO), (2007).

[6] M. R. Watts et al., Thermal Microphotonic Detection and Imaging, MSS2008

[7] M. J. Shaw, M. R. Watts, and G. N. Nielson, "Fabrication techniques for creating a thermally isolated TM-FPA (thermal microphotonic focal plane array," Proceedings of SPIE Photonics West, (2008).

[8] M. J. Shaw, J. Guo, G. A. Vawter, S. Habermehl, and C. T. Sullivan, Fabrication techniques for low loss silicon nitride waveguides, Micromachining Technology for Micro-Optics and Nano-Optics III., : Proceedings of SPIE, 2005, Vol. 5720. p. 109-118, 2005.

[9] Anthony Lawrence, *Modern Inertial technology: navigation, guidance, and control* (Springer-Verlag, New York, NY, 1998).

[10] F. Vollmer, D. Braun, A. Libchaber, M. Khoshsima, I. Teraoka, and S. Arnold, "Protein detection by optical shift of a resonant microcavity," Appl. Phys. Lett. 80, 4057 (2002)

[11] A. D. Kersey M. A. Davis, H. J. Patrick, M. Leblanc, K. P. Koo, C. G. Askins, M. A. Putnam, and E. J. Friebele, "Fibre grating sensors," *J. Lightwave Technol.* **15** 1442 (1997)

[12] R. V. Pound, "Electronic frequency stabilization of microwave oscillators," Rev. Sci. Instrum. Vol. 17, pp. 490–505 (1946)

[13] R. W. P. Drever, J. L. Hall, F. V. Kowalski, J. Hough, G. M. Ford, A. J. Munley and H. Ward, "Laser phase and frequency stabilization using an optical resonator," Applied Physics B., Vol. 31, pp. 97-105 (1983)

[14] E. Black, "An introduction to Pound-Drever-Hall laser frequency stabilization," American Journal of Physics, Vol. 69, pp. 79-87 (2001)

[15] O. Mor and A. Arie, "Performance analysis of Drever-Hall laser frequency stabilization using a proportional + integral servo," IEEE J. Quantum Electron., Vol. 33, No. 4, pp. 532-540 (1997)

Appendix A

Method of Contacting a Microring-Resonator

Microring-resonators are useful devices for filtering, sensing, modulation, and detection. In contrast to microdisks, microrings have the important property of a large free-spectral-range (FSR). However, while contacts to a microring-resonator, either mechanical and/or electrical, are essential for many applications, including sensing, modulation, and detection, doing so is complicated by the geometry of the microring. A simple contact perturbs the bend mode in the microring, inducing loss, and a significant reduction in the quality factor (Q) of the ring, limiting the utility of the microring for sensing and communications applications. To counter this problem, we propose the use of adiabatic transitions in a microring-resonator to enable lossless contacts to the microring. Doing so preserves the large FSR, high-Q, and low-loss coupling regions of the microring-resonator while enabling mechanical and/or electrical contacts to the microring.

A.1 Background

Microphotonic resonators are being increasing used for telecommunications, inter- and intra-chip communications, and sensing applications. Parameters of particular importance are the resonator quality factor or Q and the resonator free-spectral-range (FSR) or separation between resonances.

In communications applications, the resonator Q determines the bandwidth of the filtering operation that may be performed. Oftentimes this bandwidth must be very narrow in order to separate adjacent wavelength channels and minimize the impact of cross-talk between those channels. In communications applications, microring or microdisk resonators may be used to directly modulate or detect signals. In either case, the small size of the microphotonic resonator enables a vast reduction in power consumption. Yet, in order to perform either of these operations, electrical contact must be made to the resonator without corrupting the Q or FSR.

Alternatively, given their extremely high-Q, microphotonic resonators can be used for

chemical, biological, nuclear, or thermal sensing applications. Oftentimes in such sensing applications, microphotonic resonators must be isolated from their environment, yet still mechanically connected to a substrate. In doing so, the Q of the resonator must not be disturbed or the sensitivity of the sensor will be compromised. Additionally, in arrayed or distributed applications wherein many sensors are connected in series, a large FSR must be maintained since the FSR determines the number of sensors that may be connected in series.

A.2 Detailed Description of the Approach

A properly designed microring-resonator propagates only the lowest order radial, or whispering gallery type, modes. Higher order modes are precluded by the interior wall of the microring. Removal of the interior wall of the microring (Fig. A.1a) forms a microdisk (Fig. A.1b) enabling undesirable higher order modes to propagate. A comparison of the spectra of microrings and microdisks is presented in Fig. A.1c. The presence of higher order modes introduces resonances into the transmission, reflection, or absorption spectra of a microphotonic resonator. The higher order modes of a microdisk lead to a corrupted free spectral range that is about half as wide as microring (A.1c). However, while a microdisk is naturally contacted, a microring is not. The introduction of a simple contact, as depicted in Fig. A.2a, destroys the Q of the resonator. Here, a 180° bend is simulated for a ring with a direct contact. The loss in the bend was found to be 36% thereby limiting the Q of a ring with this type of contact to $Q < 2000$.

Thus, it would be desirable to enable the microring spectral and coupling features while being able to contact the microphotonic resonator as in the microdisk. To achieve the desired result, we turn to the theory of mode evolution. Mode evolution dictates that an electromagnetic mode may be slowly transitioned from one distribution to another in a lossless manner, provided that the coupling coefficients κ to the adjacent modes induced by the perturbation is small compared to the separation of the propagation constants$\Delta\ \beta$ of the adjacent modes (i.e.$\Delta\ \ \beta >> \kappa$). Simply stated, if the transition is sufficiently gradual, the transition will be losses. Thus, if an adiabatic transition is made, widening the ring prior to contact, the microring can be safely contacted with perturbing the resonant field. This is because in the widened structure, there is no field where the contact is made. This result is demonstrated in Fig. A.2b. Here, a loss of only 0.1% is found corresponding to a resonator Q of $Q \sim 10^6$ or almost three orders of magnitude greater than that of the standard contact.

Here, for the first time to our knowledge, we propose the use of an adiabatic transition within a microphotonic resonator to enable microring-like spectral qualities in a resonator that is contacted mechanically and/or electrically. The resonator takes on the form depicted in Fig. A.3a. The width of the ring waveguide is small in the region of coupling to an external bus waveguide. This narrow width ensures single-

mode, low-loss coupling to the fundamental mode of the microring. The width of the ring is the adiabatically tapered by using elliptical, oval or other gradual changes in radii to the interior or exterior walls in order to ensure a gradual, low-loss transition. Once sufficiently widened, the ring can be safely contacted without disturbing the electromagnetic field within the microring-resonator. This is possible because in the widened region where the contact is made essentially no electromagnetic field remains. This effect is depicted in Fig. A.3b. The spectra of resulting structure is depicted in Fig. A.3c. From the spectra in Fig. A.3c we see that both the FSR and Q of the resonator are maintained despite the presence of the contacts. This is in stark contrast to the directly contacted microring-resonator depicted in Fig. A.3a and its resultant spectra. The contacted region leads to radiation and loss, thereby lower the Q which is clearly seen in the extinction of the Thru Port response.

Example applications for which the importance of maintaining high-Q and large FSR is paramount are resonant modulators and detectors where electrical contacts are required (Fig. A.4a) and sensors where the microring is suspended and mechanical contact is required (Fig. A.4b).

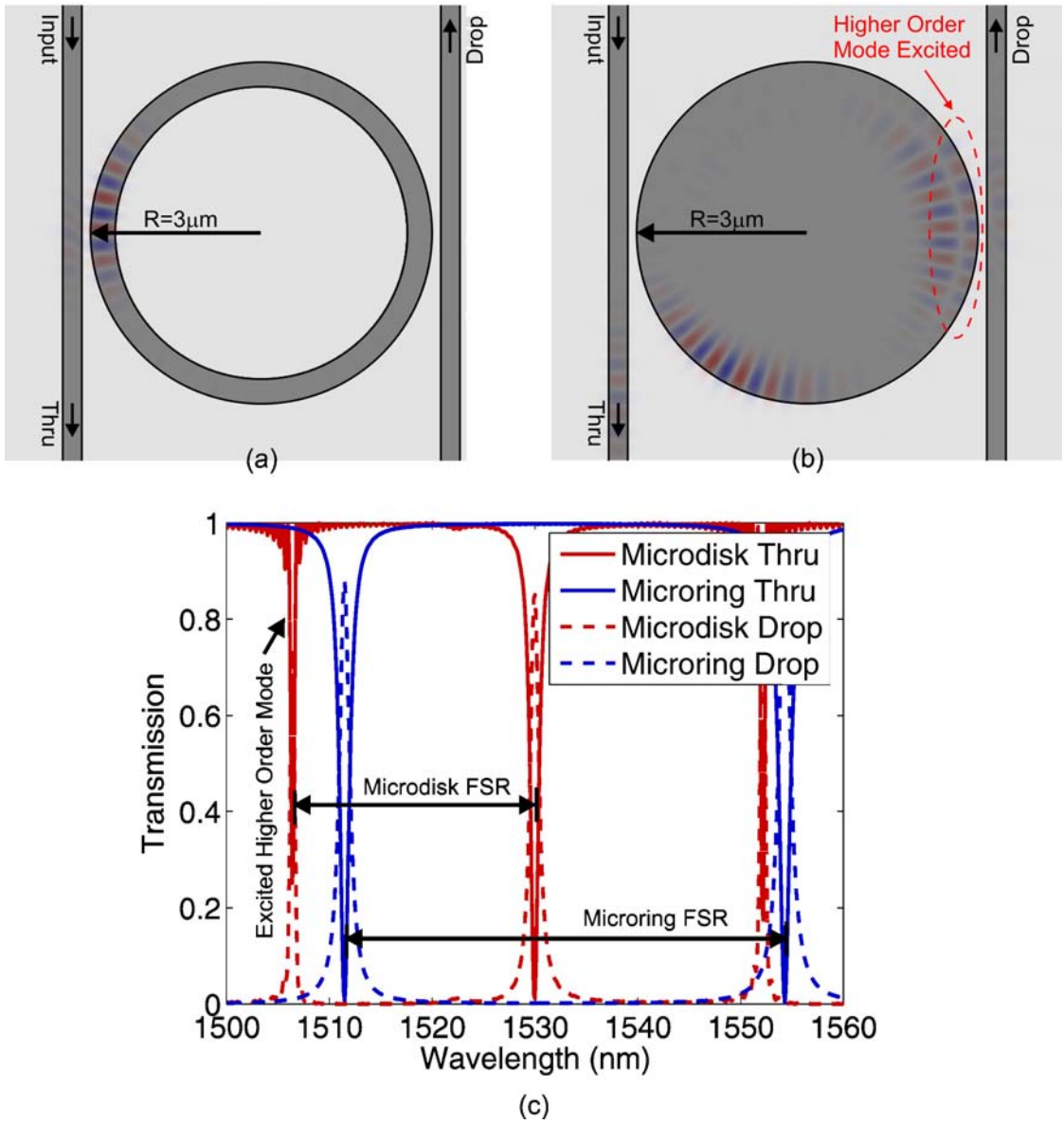

Figure A.1. (a) A Finite-Difference Time-Domain (FD-TD) simulation of a microring-resonator. The field in the bus waveguide evanescently coupled to the microring excites a single resonant spatial mode in the microring. (b) A Finite-Difference Time-Domain simulation of a microdisk-resonator. Here, the field from the bus waveguide excites both fundamental and higher order whispering gallery modes in the disk. (c) The single mode excitation in the microring leads to a clean and large free-spectral-range (FSR) in the resulting drop port spectrum while the excitation of the higher order whispering gallery modes in the microdisk leads to a cluttered spectrum that is undesirable for most applications.

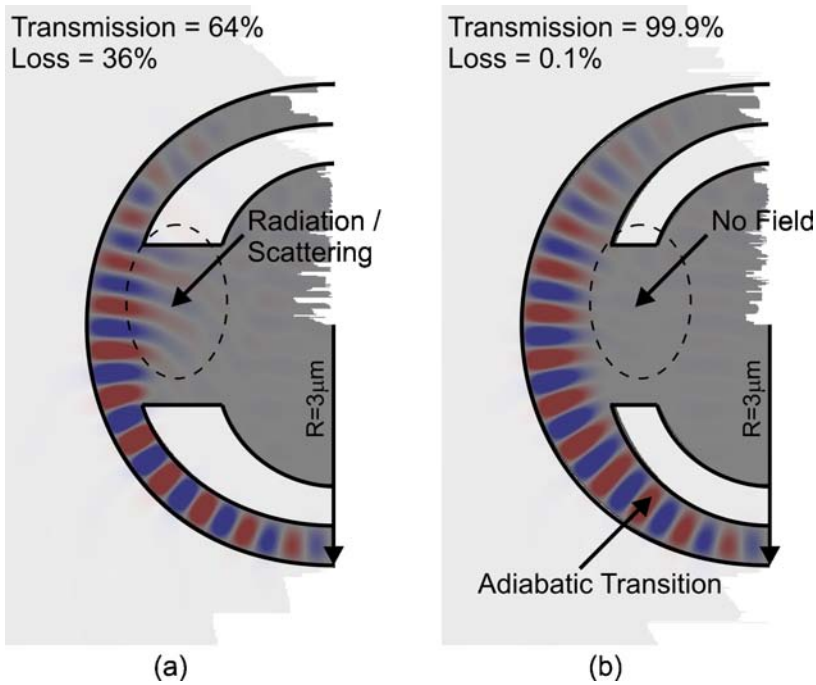

Figure A.2. FD-TD simulations of a microring resonator bend regions with (a) directly contacted and (b) adiabatically transitioned contact regions. The directly contacted microring exhibits significant radiation and loss as a result of the field interaction with the contact. The adiabatic transition eliminates this loss by first widening ring in the contact region adiabatically prior to contact. On a 180 $^\circ$ bend the loss in the standard directly contacted region (a) is 36% while in the loss in the adiabatically transitioned contact region (b), it is only 0.1%. This corresponds to almost three orders of magnitude difference in the microring-resonator Q. The Q of the standard contacted microring is only Q $<$ 2000 while that of the adiabatically contacted microring is close to 10^6.

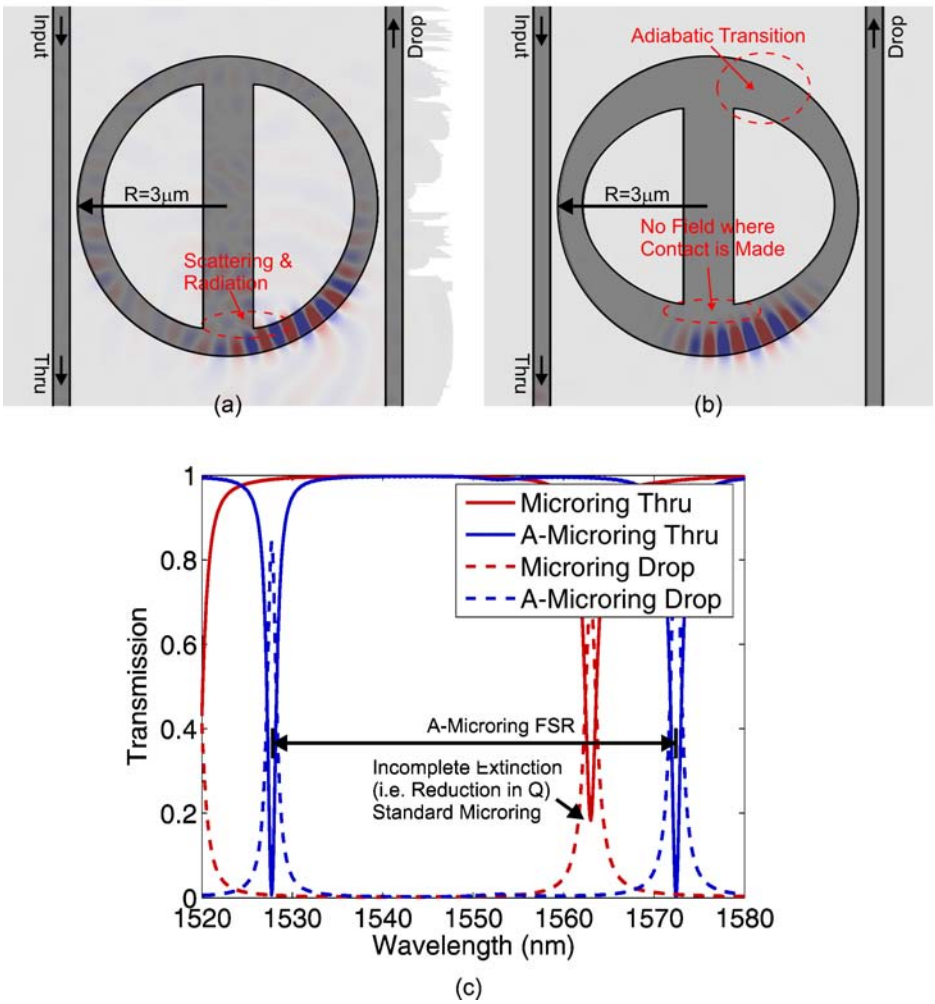

Figure A.3. (a) An FD-TD simulation of a microring resonator with a direct contact to the ring was made with excitation emanating from a bus waveguide. Here, the radiation at the interface of the contact induces radiation and loss causing a reduction in resonator Q. (b) An FD-TD simulation of an adiabatic microring or a-microring is performed. The a-microring is designed to have an adiabatic transition from a narrow ring in the coupling region to a much wider ring where the contact is made. In this configuration, the FSR of the microring is maintained without reducing the Q of the microring on account of loss at the contacts because no field is present where the contact is made. (c) The spectrum of the directly contacted and adiabatic microrings are plotted against one another. Here, we see that both have a large free spectral range, but the extinction in the standard directly contacted microring is compromised because of a reduction in Q caused by the contact.

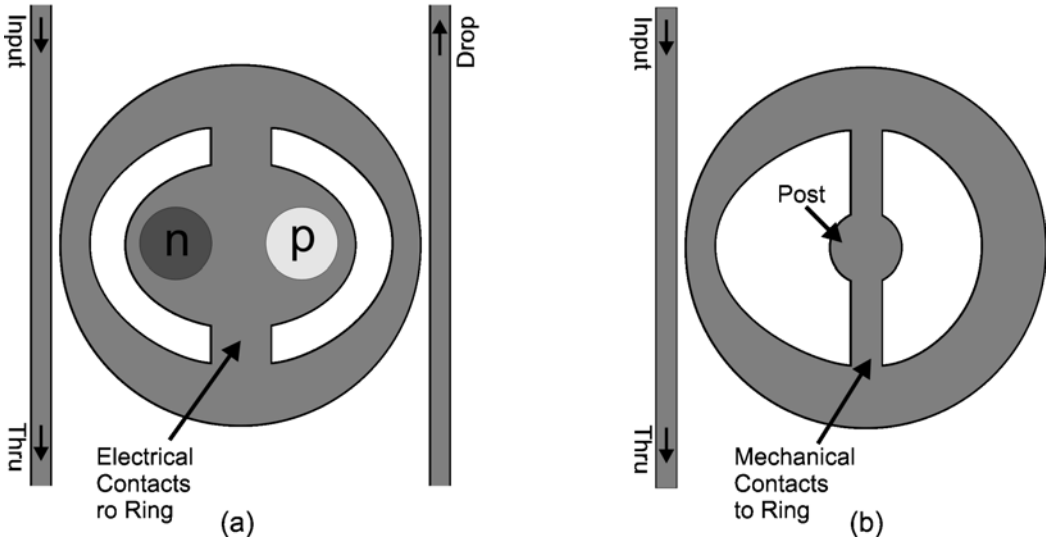

Figure A.4. Example applications of contacting a microring resonator. (a) A mechanical contact is made to a suspended microring-resonator to support the microring. Suspended microring-resonators are important for many sensing applications, including thermal, chemical, biological and nuclear. (b) An electrical contact is made to a microring resonator. Electrical contacts are important primarily for modulators and detectors in telecom and datacom applications both on and off chip.

DISTRIBUTION:

1	MS 1082	Michael R. Watts (electronic copy), 01727
1	MS 1080	Michael J. Shaw (electronic copy), 01749-1
1	MS 1082	Anthony L. Lentine (electronic copy), 01727
1	MS 1082	Peter T. Rakich (electronic copy), 01727
1	MS 1082	Jeremy B. Wright (electronic copy), 01727
1	MS 1082	Frederick B. McCormick (electronic copy), 01727
1	MS 1082	David W. Peters (electronic copy), 01727
1	MS 0123	Donna L. Chavez (electronic copy), 01011
1	MS 0980	Julie Ludwig (electronic copy), 05710
1	MS 0980	Jerome F. Jakubczak (electronic copy), 05710
1	MS 1071	Clinton A. Boye (electronic copy), 01720
1	MS 9018	Central Technical Files (electronic copy), 8944
1	MS 0899	Technical Library (electronic copy), 9536

Sandia National Laboratories